RBS and Channeling Study of Single Crystal ZnO

Aurangzib Md. Abdur Rahman

Doctor of Philosophy

Department of Electronic and Photonic Systems Engineering

Graduate School of Engineering

Kochi University of Technology

Kochi 782 8502, JAPAN.

March, 2009

RBS and Channeling Study of Single Crystal ZnO

by

Aurangzib Md. Abdur Rahman

A dissertation submitted to
Kochi University of Technology
for the partial fulfillment of the requirements
for the degree-

Doctor of Philosophy

Department of Electronic and Photonic Systems Engineering
Graduate School of Engineering
Kochi University of Technology
Kochi 782 8502, JAPAN.

March, 2009

Acknowledgement

This thesis could never be described as a solo effort, and would never have come into existence without the supervision, assistance and support provided by the following individuals. To these people I would like to extend my sincere gratitude. First of all, my principal supervisor, Professor Tadashi NARUSAWA; your enthusiasm, immense breadth of knowledge and passion for science has certainly been infectious and has very much shaped this work. I am forever grateful for being welcomed into your group. Your time and patience and interest in my work have never gone ignored. I like to offer my hearty gratitude to Dr. T NEBIKI to teach me most of the technical operations of Accelerator Lab equipments at Kochi University of Technology. I would also like to thank Dr. NEBIKI for all of the general support he has provided. To my Co-advisors, Professor Akimitsu HATTA and Professor Sadao MOMOTA, thank you for your kind cooperation.

To Professor Fumitaka NISHIYAMA of Hiroshima University, Japan- I thank you for welcoming me into your lab and giving me opportunity to perform RBS and Channeling spectrometry while our accelerator had some problem at KUT. I spent very enjoyable working time with you and appreciate the interest you showed in my work. I am grateful to Professor Takashi HIRAO and Mamoru FURUTA as well as their group of the Research Institute of Kochi University of Technology for allowing me to use their lab facilities, especially to Dr. Tokiyoshi MATSUDA and Dr. Chao Yang Li, for conducting the Photoluminescence measurements and making valuable discussions. Hall-effect measurements could not have been

conducted without the help of Dr. Tokiyoshi MATSUDA, I am really grateful for all of the support and encouragement you provided. I am also grateful to Professor Tetsuya YAMAMOTO of KUT Research Institute for giving me permission to conduct Hall-effect measurements in his lab.

To Professor Lawrence Hunter of Kochi University of Technology- I like to thank you to teach me English Research Writing. Thanks to Nissin High Voltage Company for performing ion implantation into single crystals ZnO used for this study. I am also grateful to our entire lab members, who worked with me over the years. Their friendship and kindness made me happy. I am really grateful to all of IRC members, two secretaries of Electronic and Photonic Systems Engineering Department of KUT, you gave me various supports over these three years.

Thanks to my parents whose love and encouragements were always felt, even across the miles. Finally, last, but by no means least, to my wife Rizina Momtaz and to my beloved son Wazih Taosif whose accompany in Japan kept me cheerful and energetic.

Abstract

Recently, the wide band-gap semiconductor zinc oxide (ZnO) has emerged as a potential material for the fabrication of a range of devices including optoelectronic devices such as light-emitting diodes, laser diodes and detectors. With a wide band gap of 3.37 eV and a large exciton binding energy of 60 meV at room temperature, ZnO devices will be short wavelength, operating in the blue, violet and ultra-violet regions of the spectrum, and will be applicable in such fields as medicine, high density data storage, defense and solid state lighting. Although ZnO possesses very similar properties to the nitride-based semiconductors such as GaN, it has two main advantages over this system, further enhancing its attractiveness and ensuring its position within the short-wavelength device market. Firstly, the growth of high quality single crystals of ZnO is a proven technology, (an achievement which has never been successfully overcome on a wide scale for GaN) and secondly, its large exciton binding energy (more than twice that of GaN) means that it will have a much lower power threshold for lasing by optical pumping.

The relative infancy of the field means that there is still much to be explored and understood about ZnO before such devices can be commercially realized. Most notably, *p*-type doping of ZnO remains an issue, as does the origin of the native *n*-type conductivity. These will only be resolved by a thorough understanding of the defect structure of this material. Contacts to ZnO are also a challenge which will need to be overcome before devices can be routinely produced. Aside from

these issues, there are more fundamental aspects of ZnO that still need to be explored and understood such as the response of ZnO to contact-induced damage which will invariably occur during device processing.

Ion implantation is, by definition, a destructive process. Ion implantation typically involves the irradiation of samples with ions of different species and energy. The damage profile within the irradiated sample will be dependent on the energy and mass of the incident ion, as well as other parameters such as binding energy, displacement energy and target density.

The aim of the thesis is to investigate the damage buildup behaviour in single crystal ZnO by deposition and implantation with other elements and then to draw some broad conclusions for the processing and characterization of ZnO-based devices. This has been achieved by focusing on the following: (i) the response of ZnO to contact-induced damage; (ii) investigating the influence of ion current density on damage buildup in ZnO as applicable to selective area doping by ion implantation; (iii) exploring implantation dose dependence on defects formation in ZnO; and finally (iv) focusing on the role of acceleration energy in damage production in ZnO. These aims have been achieved through a number of processes including deposition and ion-implantation and characterized using a range of techniques including Rutherford backscattering spectrometry/channeling (RBS/C), atomic force microscopy (AFM), photoluminescence (PL) and Hall-effect measurements. The crystalline quality after deposition and annealing effects on

the interface structure were investigated with RBS/C spectrometry using 2 MeV $^{4}He^{+}$ ion beam. The experimental results revealed that after Ti deposition, the minimum yield increased from 2% to 7% for substrate ZnO which indicates that damage occurred even at room temperature by deposition due to interface reaction between Ti and ZnO. After post-annealing the sample at 400 °C, it was clearly observed from the RBS/C spectra that some Zn atoms had moved on the surface.

To use ion implantation as a successful fabrication technique in materials analysis, it is necessary to understand what kinds of parameters are responsible for damage buildup. The ion beam produced lattice damage in ZnO was investigated by conducting Indium implantation into ZnO under different ion current densities, and then annealing the samples to try and recover the implantation-induced damage. The RBS/C results showed that the minimum yield, χ_{min} of the substrate ZnO single crystal increased from 2% to 22% after In^{+} implantation and the formation of bulk defect was found to be dependent on implantation ion current density. Thermal treatment after ion implantation led to improve the damage recovery. Damage was reduced to be the minimum after post-annealing the implanted sample at the highest temperature 1000 °C. RBS/C spectra also indicate that In atoms are located in the lattice site. After annealing at 1000 °C, there were no In atoms in the bulk single crystal ZnO but only had appeared on the surface. RBS/C results also suggest that there were no Indium desorption at this temperature.

Then the influence of implantation dosage on damage formation in the bulk material and its recovery were investigated by means of RBS/C and Photoluminescence studies, respectively. Three different dosages: 1Ч10^{14}, 3Ч10^{14} and 1Ч10^{15} ions.cm^{-2}, respectively were chosen for In^{+} implantation in commercial aspects. Experimental results reveal that damage buildup was found to be dependent on the dose size. The damage intensity of implanted samples gradually increased as a result of increasing ion dosage. Heat treatment after ion implantation led to improve the damage recovery as the PL intensity gradually increased with increasing temperature. However, our PL study was consistent with our RBS/C study for damage recovery. It was identified that 800 $^{\circ}$C may be the preferred annealing temperature for ZnO, as the maximum band-edge emission occurred in the same wavelength at 375 nm for both virgin and 800 $^{\circ}$C annealed samples.

Conversely, damage development under different acceleration energies and electrical properties of ZnO as a function of temperature were tried to investigate by means of RBS/C and Hall-effect measurements, respectively, however, these inconsistent results makes it difficult to reach any major conclusions, other than that there is still much work to be done in this field. Overall, the results of this thesis may be helpful for further understanding of the necessary aspects that need to be considered when undertaking ZnO-based device fabrication.

List of Figures

Figures		Page
2.1	The hexagonal wurtzite structure of ZnO	15
2.2	The rock salt and zinc blende phases of ZnO	17
2.3	The LDA band structure of bulk wurtzite ZnO	18
3.1 (a)	A Nissin 1.7 MV tandem accelerator	36
3.1 (b)	Multichannel analyzer for processing RBS/C data	36
3.1 (c)	Computer panel for receiving data from multichannel analyzer	37
3.2	A SEIKO Nanopics 2100 AFM facility	39
4.1	Experimental setup for evaluation of crystalline quality after deposition	51
4.2	Experimental setup to study Ti/ZnO interface stability	52
4.3	RBS/C spectra of Zn face (0001) oriented virgin single crystal ZnO	54
4.4 (a)	RBS/C spectra of Ti/ZnO sample (detector placed at 168°)	55
4.4 (b)	RBS/C spectra of Ti/ZnO sample (glancing angle detector placed at 100°)	55
4.5 (a)	RBS/C spectra of Ti/ZnO sample annealed at 300 °C (SSD 168°)	57
4.5 (b)	RBS/C spectra of Ti/ZnO sample annealed at 300 °C (glancing angle detector placed at 100°)	57

4.6 (a) RBS/C spectra of Ti/ZnO sample annealed at 400 °C (SSD 168°) 59

4.6 (b) RBS/C spectra of Ti/ZnO sample annealed at 400 °C (glancing angle detector placed at 100°) 59

4.7 Possible reaction mechanism of Ti/ZnO interfacial region 60

4.8 (a) AFM image of Ti deposited ZnO single crystal 62

4.8 (b) AFM image of Ti deposited ZnO single crystal, annealed at 300 °C 62

4.8 (c) AFM image of Ti deposited ZnO single crystal, annealed at 400 °C 62

5.1 Comparison of Random and channeling spectra of virgin ZnO single crystal 72

5.2 RBS/C spectra of In implanted ZnO single crystal to a dose of 1Ч10^{15} ions/cm^2 with 120 keV, while ion current density 0.7 μA/cm^2 74

5.3 RBS and aligned spectra of In implanted ZnO single crystal to a dose of 1Ч10^{15} ions/cm^2 with 120 keV, while ion current density 1.4 μA/cm^2 76

5.4 RBS/C spectra of In implanted ZnO show the damage buildup and its recovery under different ion current densities 0.7 and 1.4 μA/cm^2 77

5.5 Comparison of damage intensity with respect to ion current density in ZnO single crystal after In implantation 79

5.6 RBS/C spectra show the implanted In peaks under different annealing temperature 81

6.1	Experimental setup for RBS/C measurements using Van de Graaff accelerator to study the damage formation under different doses	91
6.2	Schematic of Photoluminescence measurements to study damage recovery of In^+ implanted single crystal ZnO	92
6.3	Random and channeling spectra of un-implanted ZnO single crystal	93
6.4	Random and channeling spectra of In^+ implanted ZnO single crystal to a dose of 1Ч10^{14} ions/cm^2 with 120 keV.	95
6.5	Random and channeling spectra of In^+ implanted ZnO single crystal to a dose of 3Ч10^{14} ions/cm^2 with 120 keV.	96
6.6	Random and channeling spectra of In^+ implanted ZnO single crystal to a dose of 1Ч10^{15} ions/cm^2 with 120 keV.	98
6.7	RBS/C spectra show the damage buildup in In^+ implanted ZnO single crystal under different dosage	100
6.8	Plot of minimum yield of In^+ implanted single crystal ZnO as a function of annealing temperature	101
6.9	RBS/C spectra show the damage recovery	102
6.10	Photoluminescence spectra of In^+ implanted ZnO single crystal show the damage recovery	104
7.1 (a)	SRIM 2003 Ion range of In implanted single crystal under an acceleration energy 60 keV	115
7.1 (b)	SRIM 2003 Ion range of In implanted single crystal under an acceleration energy 120 keV	115
7.1 (c)	SRIM 2003 Ion range of In implanted single crystal under an acceleration energy 200 keV	116

7.1 (d)	SRIM 2003 Ion range of In implanted single crystal under an acceleration energy 300 keV	116
7.2	RBS/C spectra show the depth profile of In implanted single crystal ZnO under different acceleration energies	118

List of Tables

Tables		page
1.1	Comparison of key properties between ZnO and GaN	5
3.1	MTI Corp. grown ZnO specifications	30
7.1	Some electrical properties of In Implanted single crystal ZnO	119

Table of Contents

	List of figures …………………………………………………..	vii
	List of Tables …………………………………………………..	xi
Chapter 1	**Introduction** …………………………………………………..	1
1.1	Background ………………………………………………….	2
1.2	ZnO: potential candidate for electronics and optoelectronics ...	3
1.3	Current status of the field …………………………………...	5
1.4	Aim of the work …………………………………………….	8
1.5	Thesis structure ………………………………………………..	9
1.6	References …………………………………………………..	10
Chapter 2	**Overview of ZnO: basic properties and applications …….. .**	13
2.1	Crystal structure and lattice parameters ……………………….	14
2.2	Energy band structure …………………………………………	19
2.3	Possibility of band gap engineering ……………......................	20
2.4	Mechanical properties …………………………………………	21
2.5	Electrical Properties ……………………………………………	21
2.6	Optical properties ……………………………………………...	22
2.7	Applications ………………………………………...................	23
2.8	References …………………………………………………..	25
Chapter 3	**Details of used experiments ………………………………….**	28
3.1	Samples ……………………………………………………...	29
3.2	Experimental details ………………………………………...	31
3.2.1	General concept of Rutherford Backscattering Spectrometry and Ion Channeling (RBS/C) …………………………………..	31
3.2.2	Annealing ……………………………………………………	37
3.2.3	Deposition ………………………………...........................	38
3.2.4	Atomic force microscopy ……………………………………...	38
3.2.5	Hall-effect measurements ……………………………………...	41
3.2.6	Photoluminescence …………………………………………….	42
3.2.7	Ion implantation ………………………………………………..	43
3.3	References	46

Chapter 4	**Metallic contact to ZnO** ……………………………………..	47
4.1	Introduction …………………………………………………	48
4.2	Experimental methods ………………..……........................	50
4.3	Results and discussion ………………………………………	53
4.4	Conclusion …………………………………………………..	63
4.5	References …………………………………………………..	64
Chapter 5	**Influence of ion current density on damage buildup in ZnO**	66
5.1	Introduction …………………………………………………	67
5.2	Previous studies ……………………………………………..	68
5.3	Experimental methods ………………..............................	70
5.4	Results and Discussion ……………………………………...	72
5.5	Conclusion …………………………………………………..	81
5.6	References …………………………………………………..	83
Chapter 6	**Effect of ion dose on defects formation in ZnO ……………**	87
6.1	Introduction …………………………………………………	88
6.2	Experimental methods ………………………………...........	89
6.3	Results and Discussion ……………………………………...	93
6.4	Conclusion …………………………………………………..	105
6.5	References …………………………………………………..	107
Chapter 7	**Ion beam produced damage under different acceleration energies and Hall-effect measurements ……………………..**	109
7.1	Introduction …………………………………………………	110
7.2	Experimental methods ………………………………...........	113
7.3	Results and Discussion ……………………………………...	114
7.4	Conclusion …………………………………………………..	119
7.5	References …………………………………………………..	120
Chapter 8	**Conclusions and future directions …………………………..**	122
8.1	Conclusions …………………………………………………	123
8.2	Future directions ……………………………………………	128
8.3	Closing remarks ……………………………………………..	129
	List of recent scientific publications and conferences …………	131

CHAPTER 1

Introduction

1.1 Background

Silicon has been the material of choice for integrated circuits and low power semiconductor electronic devices for the past 50 years. Scientists and engineers have studied and continue to push the limits of silicon technology meet the growing demand for advanced devices. Because of this long-standing history, silicon processing can be quite simple and inexpensive, and so it continues to be the material of choice for most applications.

Optoelectronic applications requiring light emission require the use of compound semiconductors with a direct bandgap. Traditionally this role has been dominated by GaAs, and InP compounds. More recently wide band gap semiconductor materials such as GaN or ZnO have been the subject of intense technical interest because with their wide band gap they can emit light in the visible and ultraviolet. This has resulted in commercialization of visible LEDs, blue and ultraviolet lasers and ultraviolet photodetectors. Wide band gap semiconductors are also increasingly being used in high power electronics such as solid state amplifiers and switches.

For extreme environments, such as outer space, radiation hardness can be a critical quality for devices since device performance can be significantly altered by the constant bombardment of energetic particles and electromagnetic

radiation. Parameters such as threshold voltage, leakage current and saturation current that are critical to proper device performance may change significantly with a sufficient dose of ionizing radiation, which may cause equipment malfunction or failure. Materials such as ZnO or InP have been demonstrated to be more resistant to radiation damage than other semiconductors such as silicon and GaAs.

1.2 ZnO: Potential candidate for electronics and optoelectronics

Zinc oxide (ZnO) is no stranger to scientific study. In the past ～100 years, it has featured as the subject of thousands of research papers, dating back as early as 1935 [1]. Valued for its ultra violet absorbance, wide chemistry, piezoelectricity and luminescence at high temperatures, ZnO has penetrated far into industry, and is one of the critical building blocks in todays modern society [2]. It can be found in paints, cosmetics, plastic and rubber manufacturing, electronics and pharmaceuticals, to name just a few. More recently however, ZnO has again entered the scientific spotlight, this time for its semiconducting properties [3]. Fueled out of advances in growth technologies and the potential for ZnO to become a suitable substrate for GaN, the fabrication of high quality single crystals and epitaxial layers was achieved [4, 5]. This development heralded a new era for ZnO, allowing for the

realisation of ZnO-based photonic and optoelectronic devices, where, amongst other potential applications it stands with GaN as a prospective candidate for the next generation of light emitters for solid state lighting applications [6, 7]. With a wide band gap of 3.4 eV and a large exciton binding energy of 60 meV at room temperature, ZnO holds excellent promise for blue and ultra-violet optical devices.

Although in the past GaN and GaN-based materials have dominated this wavelength range, ZnO enters the arena with several advantages [3, 6]. The two most crucial of these are:

1. the larger exciton binding energy, which will allow for room temperature devices operating with higher efficiency and lower power threshold for lasing by optical pumping
2. the ability to grow high quality single crystal substrates with relative cost effectiveness and ease - something that still eludes GaN

Table 1.1 highlights some of the key properties of ZnO, and provides a comparison with GaN. Other favourable aspects of ZnO include its broad chemistry leading to many opportunities for wet chemical etching, piezoelectric properties, radiation hardness and high ferromagnetic Curie temperature for spintronic applications [8–11]. Together, these properties make

ZnO an ideal candidate for a variety of devices including blue and ultra-violet laser diodes and light emitting diodes [12].

Table 1.1: ZnO and GaN: key properties compared

Property	**ZnO**	**GaN**
Energy band gap, E_g (eV)	3.37	3.4
RT exciton binding energy, E_B (meV)	60	21~28
RT stable phase	Wurtzite	Wurtzite
a_o (E)	3.25	3.12
c_o (E)	5.21	5.19
Bulk growth	Yes	Difficult
Epitaxial growth	Yes	Yes

1.3 Current status of the field

Despite the maturity of the field of semiconductors and the wide information base available for ZnO; as a semiconductor, little is actually known about this material. As with all wide band-gap semiconductors, ZnO has presented a number of hurdles to the scientific community which need to be understood and overcome before ZnO based devices can be commercially realized. This thesis comes in what could be described as the 'teenage years' of research into

ZnO devices. The teething problems that initially hindered the realization of ZnO devices have been overcome. These would include mainly growth advances, which have seen the development of reproducible high quality epitaxial layers and single crystals [4, 5].

Doping of ZnO has also proved to be an enduring challenge in this material system, something not uncommon for wide band gap semiconductors [13]. Although ZnO is predicted to be an intrinsic semiconductor, it naturally occurs as *n*-type, with a concentration of $\sim 10^{16}$ cm^{-3} for typical high-quality material. The origin of this *n*-type conductivity is still a controversy, with significant studies (both experimental and theoretical) being conducted which fail to reach a consistent resolution. The dominant donor was thought to be a native defect, with O vacancies (V_o) and Zn interstitials (I_{Zn}) projected to have donor behaviour [14]. Of these, V_o has been found to be a deep donor, and I_{Zn} a shallow one [15], whilst both have relatively high formation energies [16]. The deep level of V_o and the high formation energies of both defects mean that both independently or combined, these defects alone cannot account for the very high electron concentration in as-grown ZnO. Hydrogen (which is virtually impossible to eliminate during growth, particularly of bulk material) has also been implicated as a shallow donor in ZnO [17], although it alone also fails to account for this level of conductivity. More recently, there is a trend to attribute this native conductivity to group III impurities such as Al and Ga

along with H as the dominant donors in ZnO [18]. Al is often used as a *n*-type dopant in ZnO, and is renowned for producing highly *n*-conductive layers, as well as being a common contaminant in the ZnO system. The search for definitive confirmation of the donor(s) in this system thus remains. Although the understanding of the processes responsible for the background doping in ZnO is incomplete, unsurprisingly even less is known about acceptors in this material. Frustratingly, whilst reports of *p*-type ZnO are emerging (for example [19–22]) their reliability and reproducibility is at best questionable, most likely due to stability issues. For this reason, the achievement of reliable and reproducible *p*-type ZnO has so far mostly eluded researchers. Obviously, this is an absolutely critical point to be overcome if ZnO based devices are ever to become a viable reality.

Having said this however, electroluminescence from a ZnO homojunction has been recently reported [23], suggesting that with persistence *p*-type ZnO will be routinely realized. The group V elements N, As, P and Sb are widely hailed as the most promising candidates for acceptors in this material. Aside from the doping issues, Schottky contact formation on ZnO has also been plagued by difficulties. Good quality electrical contacts are crucial not only for device manufacture, but also for a range of electrical characterization techniques, such as capacitance-voltage profiling, deep level transient spectroscopy (DLTS). Such techniques are invaluable for providing information about the carriers

and defect states within materials, and would be an ideal complement to defect studies in ZnO. Until reliable Schottky diodes that are not ’leaky’ can be produced however, such techniques are not available to researchers [24]. Like the doping issues in ZnO, this difficulty in forming metallic contacts to ZnO arises due to surface states that still remain unidentified [24,25].

1.4 Aim of the work

At the current point in time there is still much to be understood about ZnO before devices can become commercially viable, particularly in relation to defect states in the material, and the effect these have on conductivity and band edge emission. The motivation of this thesis is thus to process and characterize ZnO whilst monitoring the ion beam produced lattice damage. Specifically the effects of contact induced damage on ZnO surfaces, and damage buildup behaviour by ion implantation. It is hoped that the results presented within this thesis will help the field move, at least a small way, towards ZnO device processing and fabrication.

1.5 Thesis structure

The thesis is structured as follows: Chapter 2 gives an overview of some of the basic properties of ZnO that are already known and have some background relevance to this thesis.

All sample details and a brief description of each of the experimental techniques used are presented in chapter 3. Chapters 4 – 7 deal with the results from my own studies. These chapters are each structured to provide an introduction to the topic, including a literature review on the field to place the work into context, followed by specific experimental details, results, discussions and conclusions. Specifically, Chapter 4 deals with a study of metallic contact on ZnO and interface stability. Chapter 5 deals with the influence implantation ion current density on defects generation in ZnO. Chapter 6 explores the dose dependence on damage formation and recovery in ion implanted ZnO. Chapter 7 deals with the impact of acceleration energy on damage buildup in ZnO, and shows the results of Hall-effect measurements in trying to study the electrical properties of ZnO.

Finally, in chapter 8 some general conclusions for all of the work are drawn and avenues for possible future directions of study are projected.

1.6 References

[1] C. W. Bunn, "The lattice-dimensions of zinc oxide," *Proc. Phys. Soc. London* **47,** 835 (1935).

[2] D. R. Lide (editor), *CRC Handbook of Chemistry and Physics*, CRC Press, New York, 73rd edition, 1992.

[3] D. C. Look, "Recent advances in ZnO materials and devices," *Mat. Sci. Eng. B.* **80,** 383 (2001).

[4] D. C. Look, D. C. Reynolds, J. R. Sizelove, R. L. Jones, C. W. Litton, G. Cantwell and W. C. Harsch, "Electrical properties of bulk ZnO," *Solid State Commun.* **105,** 399 (1998).

[5] Y. Segawa, A. Ohtomo, M. Kawasaki, H. Koinuma, Z. K. Tang, P. Yu and G. K. L. Wong, "Growth of ZnO thin films by laser-MBE: Lasing of excitons at room temperature," *Phys. Stat. Sol.* **202,** 669 (1997).

[6] J. E. Nause, "ZnO broadens the spectrum," *III-Vs Review* **12,** 28 (1999).

[7] J. E. Nause, "Fluorescent substrate offers route to phosphor-free LEDs," *Comp. Semicond.* **11,** 29 (2005).

[8] S. O. Kucheyev, J. S. Williams, C. Jagadish, J. Zou, C. Evans, A. J. Nelson and A. V. Hamza, "Ion-beam-produced structural defects in ZnO," *Phys. Rev. B* **67,** 094 115 (2003).

[9] C. Coskun, D. C. Look, G. C. Farlow and J. R. Sizelove, "Radiation hardness of ZnO at low temperatures," *Semicond. Sci. Technol.* **19,** 752 (2004).

[10] S. O. Kucheyev, J. S. Williams and C. Jagadish, “Ion-beam-defect processes in group-III nitrides and ZnO,” *Vacuum* **73,** 93 (2004).

[11] N. A. Spaldin, “Search for Ferromagenetism in transition-metal-doped piezoelectric ZnO,” *Phys. Rev. B* **69,** 125 201 (2004).

[12] S. J. Pearton, D. P. Norton, K. Ip, Y. Heo and T. Steiner, *J. Vac. Sci. Technol. B* **22,** 932 (2004).

[13] D. C. Look and B. Claflin, *Phys. Stat. Sol. (b)***241,** 624 (2004).

[14] D. C. Look, B. Claflin, Y. I. Alivov and S. J. Park, *Phys.Stat. Sol. (a)* **201,** 2203 (2004).

[15] S. B. Zhang, S. H. Wei and A. Zunger, *Phys. Rev. B* **63,** 075 205 (2001).

[16] A. F. Kohan, G. Ceder, D. Morgan and C. G. Van deWalle, *Phys. Rev. B* **61,** 15 019 (2000).

[17] C. G. Van de Walle, *Phys. Rev. Lett.* **85,** 1012 (2000).

[18] D. C. Look, *Semicond. Sci. Technol.* **20,** S55 (2005).

[19] G. Xiong, J.Wilkinson, B.Mischuck, S. Tuzemen, K. B. Ucer and R. T.Williams, *Appl. Phys. Lett.* **80,** 1195 (2002).

[20] D. C. Look, D. C. Reynolds, C. W. Litton, R. L. Jones, D. B. Eason and G. Cantwell, *Appl. Phys. Lett.* **81,** 1830 (2002).

[21] A. V. Singh, R. M. Mehra, A. Wakahara and A. Yoshida, *J. Appl. Phys.* **93,** 396 (2003).

[22] Y. R. Ryu, T. S. Lee and H. W. White, *Appl. Phys. Lett.* **83,** 87 (2003).

[23] A. Tsukazaki, A. Ohtomo, T. Onuma, M. Ohtani, T. Makino, M. Sumiya, K. Ohtani, S. F. Chichibu, S. Fuke, Y. Segawa, H. Ohno, H. Koinuma and M. Kawasaki, *Nat. Mat.* **4,** 42 (2005).

[24] U. Grossner, S. Gabrielsen, T. M. Bшrseth, J. Grillenberger, A. Y. Kuznetsov and B. G. Svensson, *Appl. Phys. Lett.* **85**: 2259, 2004.

[25] B. J. Coppa, C. C. Fulton, S.M. Kiesel, R. F. Davis, C. Pandarinath, J. E. Burnette, R. J. Nemanich and D. J. Smith, *J. Appl. Phys.* **97,** 103 517 (2005).

CHAPTER 2

Overview of ZnO: basic properties and applications

2.1 Crystal structure and lattice parameters

At ambient pressure and temperature, ZnO crystallizes in the wurtzite (B4 type) structure, as shown in figure 2.1. This is a hexagonal lattice, belonging to the space group P63*mc*, and is characterized by two interconnecting sub-lattices of Zn^{2+} and O^{2-}, such that each Zn ion is surrounded by a tetrahedral of O ions, and vice-versa. This tetrahedral coordination gives rise to polar symmetry along the hexagonal axis. This polarity is responsible for a number of the properties of ZnO, including its piezoelectricity and spontaneous polarization, and is also a key factor in crystal growth, etching and defect generation. The four most common face terminations of wurtzite ZnO are the polar Zn terminated (0001) and O terminated (000Y1) faces (*c*-axis oriented), and the non-polar (11Y20) (*a*-axis) and (10Y10) faces which both contain an equal number of Zn and O atoms. The polar faces are known to possess different chemical and physical properties, and the O-terminated face possesses a slightly different electronic structure to the other three faces [1]. Additionally, the polar surfaces and the (10Y10) surface are found to be stable; however the (11Y20) face is less stable and generally has a higher level of surface roughness than its counterparts. The (0001) plane is also basal.

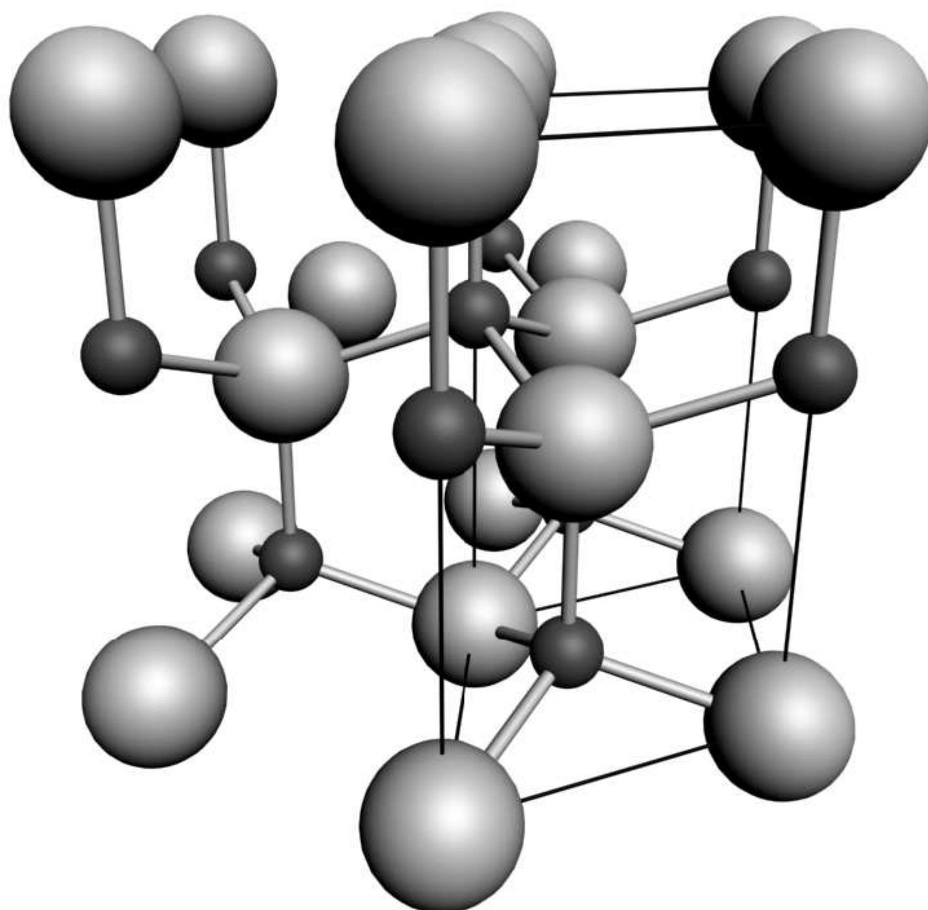

Figure 2.1: The hexagonal wurtzite structure of ZnO. O atoms are shown as larger white spheres, Zn atoms as smaller black spheres. One unit cell is outlined for clarity.

Aside from causing the inherent polarity in the ZnO crystal, the tetrahedral coordination of this compound is also a common indicator of sp^3 covalent bonding. However, the Zn - O bond also possesses very strong ionic character, and thus ZnO lies on the borderline between being classed as a covalent and ionic compound, with an ionicity of $f_i = 0.616$ on the Phillips ionicity scale [2]. The lattice parameters of the hexagonal unit cell are $a = 3.2495$ E and $c = 5.2069$ E, and the density is 5.605 gcm^{-3} [3].

Additional to the wurtzite phase, ZnO is also known to crystallize in the zinc blende and cubic rocksalt (NaCl) structures, which are illustrated in figure 2.2. Zinc blende ZnO is stable only by growth on cubic structures [4–6], whilst the rocksalt structure is a high-pressure metastable phase forming at ～10 GPa, and cannot be epitaxially stabilized [7]. Theoretical calculations indicate that a fourth phase, cubic caesium chloride, may be possible at extremely high temperatures, however, this phase has yet to be experimentally observed [8].

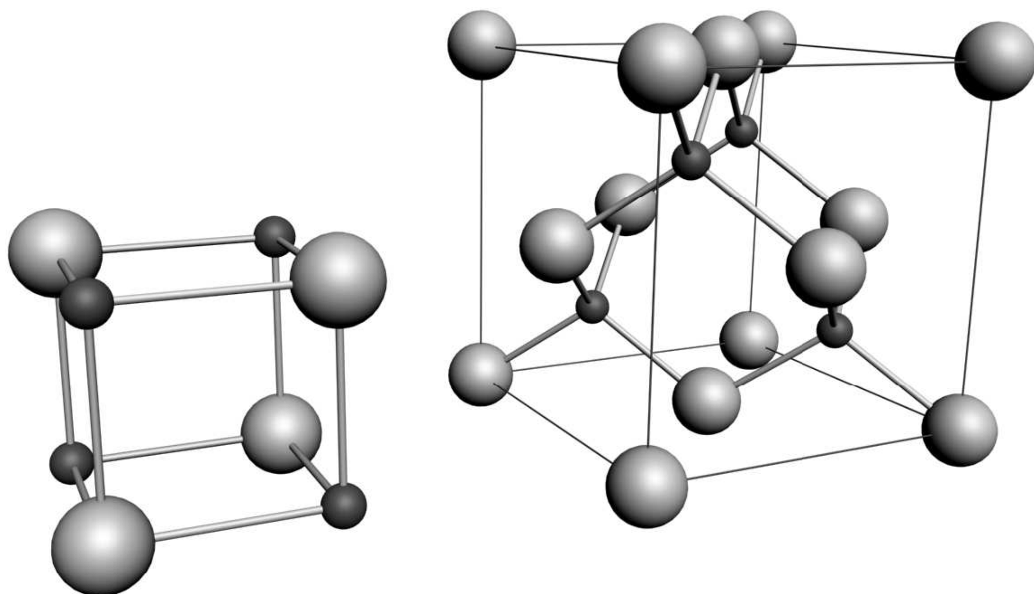

Figure 2.2: The rock salt (left) and zinc blende (right) phases of ZnO. O atoms are shown as white spheres, Zn atoms as black spheres. Only one unit cell is illustrated for clarity.

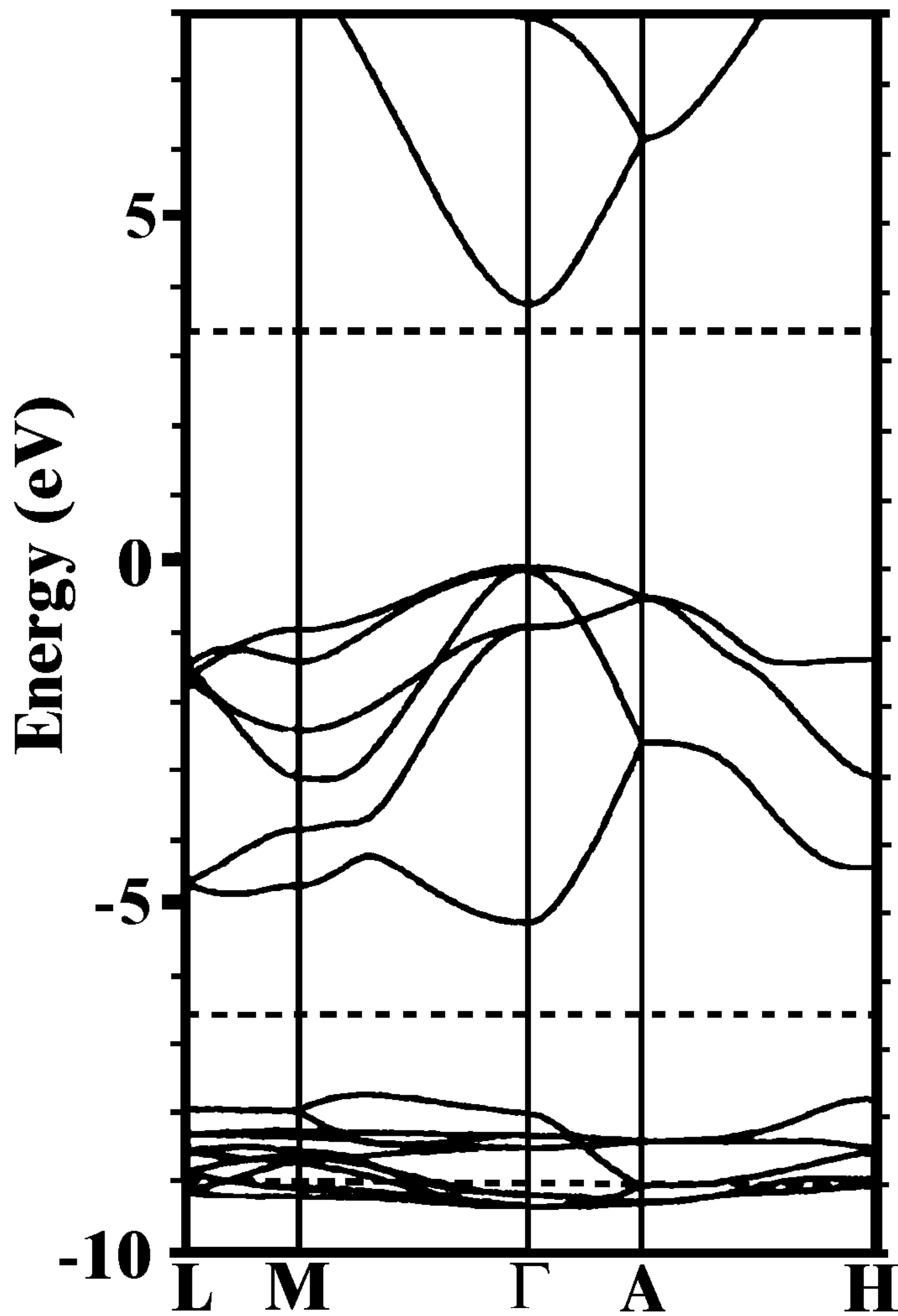

Figure 2.3: The LDA band structure of bulk wurtzite ZnO calculated using dominant atomic self-interaction-corrected pseudopotentials (SIC-PP). From: *D. Vogel, P. KrËuger and J. Pollmann, Phys. Rev. B* ***52****, R14316 (1995).*

2.2 Energy band structure

The electronic band structure of ZnO has been calculated by a number of groups [8–14]. The results of a band structure calculation using the Local Density Approximation (LDA) and incorporating atomic self-interaction corrected pseudopotentials (SIC-PP) to accurately account for the Zn 3*d* electrons is shown in figure 2.3 [14]. The band structure is shown along high symmetry lines in the hexagonal Brillouin zone. Both the valence band maxima and the lowest conduction band minima occur at the Γ point k = 0 indicating that ZnO is a direct band gap semiconductor. The bottom 10 bands (occurring around -9 eV) correspond to Zn 3*d* levels. The next 6 bands from -5 eV to 0 eV correspond to O 2*p* bonding states. The first two conduction band states are strongly Zn localized and correspond to empty Zn 3*s* levels. The higher conduction bands are free-electron-like. The O 2*s* bands associated with core-like energy states, occur around -20 eV. The band gap as determined from this calculation is 3.77 eV. This correlates reasonably well with the experimental value of 3.4 eV, and is much closer than the value obtained from standard LDA calculations, which tend to underestimate the band gap by ～3 eV due to its failure in accurately modeling the Zn 3*d* electrons.

In addition to calculations for the band structure of bulk ZnO, Ivanov and Pollmann have also carried out an extensive study on the electronic structure of

the surfaces of wurtzite ZnO [13]. Using the empirical tight-binding method (ETBM) to determine a Hamiltonian for the bulk states, the scattering theoretical method was applied to determine the nature of the surface states. The calculated data was found to be in very good agreement with experimental data obtained from electron-energy-loss spectroscopy (EELS) and ultra-violet photoelectron spectroscopy (UPS). As discussed in section 2.1, the properties of the two polar faces are expected to be different, Zn face possesses more covalent character, arising from the Zn 4*s* - O 2*p* states, whilst the O face is more ionic.

2.3 Possibility of band gap engineering

For a semiconductor to be useful, particularly in reference to optoelectronic devices; band gap engineering is a crucial step in device development. By alloying the starting semiconductor with another material of different band gap, the band gap of the resultant alloy material can be fine tuned, thus affecting the wavelength of exciton emissions. In the case of ZnO, alloying with MgO and CdO is an effective means of increasing or decreasing the energy band gap, respectively [15–17]. Currently however, due to the infancy of the field, only limited experimental and theoretical work has been done for these materials, and thus the information available is both incomplete and not well verified.

2.4 Mechanical properties

ZnO is a relatively soft material, with a hardness of ～5 GPa at a plastic penetration depth of 300 nm [18]. This needs to be taken into consideration when processing and designing ZnO based devices. Nanoindentation is a useful technique for probing the mechanical properties of a material, whilst also providing information on the behaviour of a material under contact induced damage, such as that experienced during device processing. For ZnO, indentation results in significant quenching of the excitonic luminescence. Additionally, extensive damage is created in the ZnO material, with defects propagating far beyond the volume under contact [19]. Piezoelectricity is also an important mechanical property. ZnO is believed to have a piezoelectric tensor equal to or even greater than that of GaN and AlN, which means that ZnO is a suitable candidate for device applications requiring a large electromechanical coupling [20].

2.5 Electrical properties

The electrical properties of ZnO are hard to quantify due to large variance of the quality of samples available. The background carrier concentration varies a lot according to the quality of the layers but is usually within the range 10^{15} - ～10^{17} cm^{-3}. The largest reported *n*-type doping is ～10^{20} electrons/cm^3 and largest reported *p*-type doping is ～10^{19} holes/cm^3, however such high levels of

p-conductivity are questionable and have not been experimentally verified [21]. The exciton binding energy is 60 meV at 300K, and is one of the reasons why ZnO is so attractive for optoelectronic device applications. As it is already known that the electron effective mass is $0.24m_o$, and the hole effective mass is $0.59m_o$. The corresponding electron Hall mobility at 300K for low *n*-type conductivity is μ = 200 $cm^2\ V^{-1}\ s^{-1}$, and for low *p*-type conductivity is in the range of 5-50 $cm^2\ V^{-1}\ s^{-1}$ [22].

2.6 Optical properties

The optical properties of ZnO are heavily influenced by the energy band structure and lattice dynamics. For a comprehensive review of the optical properties of excitonic recombinations in bulk, *n*-type ZnO, please refer to the work of B. K. Meyer *et. al.* [23]. This work gives a comprehensive treatment and analysis of the excitonic spectra obtained from ZnO, and assigns many defect related spectral features, as well as donor-acceptor pair (DAP) emission. A broad defect related peak extending from ～1.9 to ～2.8 eV is also a common optical feature of ZnO. Known as the green band, the origin of its luminescence is still not well understood and has in the past been attributed to a variety of different impurities and defects. A typical photoluminescence spectra of *n*-type ZnO usually clearly show excitonic, DAP and extended green band emission, as well as phonon replicas produced from the longitudinal optical phonons (LO). In terms of the more fundamental optical properties of

ZnO, there have been a number of comprehensive studies to determine the refractive index and dielectric constants of this material [24–26].

2.7 Applications

In this section, a brief overview of the projected applications for ZnO is provided. As mentioned in Chapter 1, ZnO is already widely used in our society. With improvements in growth technology of ZnO nanostructures, epitaxial layers, single crystals and nanoparticles, we are now moving into an era where ZnO devices will become increasingly functional and exotic. ZnO-based nanostructures including nanowire arrays hold a host of opportunities for flat screen displays, field emission sources, gas, chemical [27] and biological sensors, and as UV light emitters, detectors and switches [27–30]. Epitaxial layers and single crystals will be important for the development of optoelectronic (blue and ultraviolet light emitters and detectors) [31], piezoelectric [32] and spintronic [33] devices, and together with GaN may form the light source of the 21st century [34]. Such devices also have applications within defence, ultra high density data storage, blue, UV and white light LED's and laser diodes, secure communications and biodetection. Epitaxial ZnO also holds much promise as a semiconducting transparent thin film [35], which again will be important for solar cells, gas sensors, UV detectors, displays and wavelength selective applications. Existing technologies are also being revolutionized with ZnO nanoparticles, which have

led to the development of improved sunscreens, paints and coatings to name just a few.

Additionally, the radiation hardness of ZnO to MeV proton irradiation makes it an ideal candidate for space applications [36]. Thus ZnO whilst already possessing a wide application base, has enormous opportunities for society and industry alike due to its unique properties which are now being explored and applied.

2.8 References

[1] O. Dulub, L. A. Boatner and U. Diebold, *Surf. Sci.* **519,** 201 (2002).

[2] J. C. Phillips, *Bonds and Bands in Semiconductors*, Academic, New York, 1973.

[3] D. R. Lide (editor), *CRC Handbook of Chemistry and Physics*, CRC Press, New York, 73rd edition, 1992.

[4] T. Kogure and Y. Bando, *J. Electron Microsc.* **47**, (1998).

[5] A. B. M. A. Ashrafi, A. Ueta, A. Avramescu, H. Kumano, I. Suemune, Y. W. Ok and T. Y. Seong, *Appl. Phys. Lett.* **76,** 550 (2000).

[6] S. K. Kim, S. Y. Jeong and C. R. Cho, *Appl. Phys. Lett.* **82,** 562 (2003).

[7] C. H. Bates, W. B. White and R. Roy, *Science* **137,** 993 (1962).

[8] J. E. Jaffe, J. A. Snyder, Z. Lin and A. C. Hess, *Phys. Rev. B* **62,** 1660 (2000).

[9] J. R. Chelikowsky, *Sol. Stat. Comm.* **22,** 351 (1977).

[10] U. RËossler, *Phys. Rev.* **184,** 733 (1969).

[11] S. Bloom and I. Ortenburger, *Phys. Stat. Sol. (b)***58,** 561 (1973).

[12] M. Usuda, N. Hamada, T. Kotani and M. van Schilfgaarde, *Phys. Rev. B* **66,** 125 101 (2002).

[13] I. Ivanov and J. Pollmann, *Phys. Rev. B* **24,** 7275 (1981).

[14] D. Vogel, P. KrËuger and J. Pollmann, *Phys. Rev. B* **52,** R14 316 (1995).

[15] T. Makino, C. H. Chia, N. T. Tuan, H. D. Sun, Y. Segawa, M. Kawasaki, A. Ohtomo, K. Tamura and H. Koinuma, *Appl. Phys. Lett.* **77,** 975 (2000).

[16] K. Ogata, K. Koike, T. Tanite, T. Komuro, F. Yan, S. Sasa, M. Inoue and M. Yano, *J. Cryst. Growth* **251,** 623 (2003).

[17] T. Makino, Y. Segawa, M. Kawasaki, A. Ohtomo, R. Shiroki, K. Tamura, T. Yasuda and H. Koinuma, *Appl. Phys. Lett.* **78,** 1237 (2001).

[18] S. O. Kucheyev, J. E. Bradby, J. S. Williams, C. Jagadish and M. V. Swain, *Appl. Phys. Lett.* **80,** 956 (2002).

[19] J. E. Bradby, S. O. Kucheyev, J. S. Williams, C. Jagadish, M. V. Swain, P. Munroe and M. R. Philips, *Appl. Phys. Lett.* **80,** 4537 (2002).

[20] A. Dal Corso, M. Posternak, R. Resta and A. Baldereschi, *Phys. Rev. B* **50,** 10 715 (1994).

[21] D. C. Look, B. Claflin, Y. I. Alivov and S. J. Park, *Phys. Stat. Sol. (a)* **201,** 2203 (2004).

[22] S. J. Pearton, D. P. Norton, K. Ip, Y. W. Heo and T. Steiner, *Prog. in Mater. Sci.* **50,** 293 (2005).

[23] B. K. Meyer, H. Alves, D. M. Hofmann, W. Kriegseis, D. Forster, F. Bertram, J. Christen, A. Hoffmann, M. Straburg, M. Dworzak, U. Haboeck and A. V. Rodina, *Phys. Stat. Sol. (b)* **241,** 231 (2004).

[24] H. Yoshikawa and S. Adachi, *Jpn. J. Appl. Phys.* **36,** 6237 (1997).

[25] N. Ashkenov, Mbenkum B, M, C. Bundesmann, V. Riede, M. Lorenz, D. Spemann, E. M. Kaidashev, A. Kasic, M. Schubert, M. Grundmann, G. Wanger, H. Neumann, V. Darakchieva, H. Arwin and B. Monemar, *J. Appl. Phys.* **93,** 126 (2003).

[26] X. W. Sun and H. S. Kwok, *J. Appl. Phys.* **86,** 408 (1999).

[27] L. Liao, J. C. Li, D. F. Wang, C. Liu, C. S. Liu, Q. Fu and L. X. Fan, *Nanotech.* **16,** 985 (2005).

[28] Y. Xia, P. Yang, Y. Sun, Y. Wu, B. Mayers, B. Gates, Y. Yin, F. Kim and H. Yan, *Adv. Mat.* **15,** 353 (2003).

[29] Z. L. Wang, *J. Phys.Cond. Mat.* **16,** R829 (2004).

[30] D. J. Sirbuly, M. Law, H. Q. Yan and P. D. Yang, *J. Phys. Chem. B* **109,** 15 190 (2005).

[31] D. C. Look, *Mat. Sci. Eng. B.* **80,** 383 (2001).

[32] J. G. E. Gardeniers, Z. M. Rittersma and G. J. Burger, *J. Appl. Phys.* **83,** 7844 (1998).

[33] D. P. Norton, S. J. Pearton, A. F. Hebard, N. Theodoropoulou, L. A. Boatner and R. G. Wilson, *Appl. Phys. Lett.* **82,** 239 (2003).

[34] J. E. Nause, *Comp. Semicond.* **11,** 29 (2005).

[35] H. Hartnagel, A. L. Dawar, A. K. Jain and C. Jagadish, *Semiconducting transparent thin films*, Institute of Physics Publishing, Bristol and Philadelphia, 1995.

[36] C. Coskun, D. C. Look, G. C. Farlow and J. R. Sizelove, *Semicond. Sci. Technol.* **19,** 752 (2004).

CHAPTER 3

Details of used Experiments

3.1 Samples

The samples used in this thesis were all acquired externally. The details of the samples, their source, growth method, and properties are provided in the subsection below.

MTI Corp.

www.mticrystal.com

The bulk ZnO samples used in this thesis were purchased fromMTI Corp, a crystal growth company from the USA. ZnO crystals are manufactured by the hydrothermal technology. Its advantage is the size of the grown crystals and excellent quality. A detailed description of this process can be found in literature [1], however the main concepts of the growth will be presented here. Growing ZnO by hydrothermal method is quite a slow process, which allows to achieve a very high quality of the crystal, without block marks, twins and dislocations. Hydrothermal ZnO single crystals are grown in high pressure autoclaves by means of direct temperature drop in aqueous solutions of KOH + LiOH at crystallization temperature 320- 400 °C and pressure 20-70 MPa. Inside the autoclaves there are special vessels made of corrosion-resistant alloys – they serve to protect autoclaves from corrosion. The charge, the bait and the chemical solution are put into the vessel, then the vessel is hermetically sealed and placed into the autoclave. Finally the autoclave is filled with water and is also sealed hermetically. After that the autoclave is heated to the fixed

temperature. The whole production cycle takes 100-150 days. Table 3.1 shows the typical specifications of MTI ZnO wafers.

Table 3.1: MTI Corp. grown ZnO specifications

Purity wt% Impurity: wt%	> 99.99 Mg: <.0005 Al: < .0030 Si: 0.0030 Ti: .0010 Cu: < .0030 Fe: < 0.005 Ca: <.0005 Ag: < .0002
Crystal Structure	Hexagonal: a= 3.252 e , c = 5.313 e
Growth Method	Hydrothermal
Hardness	4 moh scale
Density	5.7 g/cm^3
Melt Point	1975 ^{o}C
Specific heat	0.125 cal/gm
Thermoelectric Constant	1200 μV /^{o}K @ 300 ^{o}C
Thermal conductivity	0.006 cal/cm/ ^{o}K
Thermal expansion	2.90 x 10-6/^{o}K
Transmission range	0.4 - 0.6 μ > 50% at 2 mm
Dislocation Density	<0001> plane <100 / cm^2

3.2 Experimental details

This section deals with the main experimental characterization techniques that make up the work presented in this thesis. These are Rutherford Backscattering Spectrometry and Channeling (RBS), Atomic Force Microscopy (AFM), Photoluminescence (PL) and Hall-effect measurements. Details of equipment used for processing, including ion implantation, annealing, deposition are also provided. These are all well established experimental techniques, the details of which can be easily found in text books and on the internet. As such, this chapter serves to provide a very general overview of the main principles and applications of the techniques, as relevant to the work presented in this thesis only. Specific experimental details will be given throughout the remainder of the thesis as required.

3.2.1 General concept of Rutherford backscattering spectrometry and Ion Channeling (RBS/C)

Rutherford backscattering spectrometry/channeling is a well established technique based on collisions between atomic nuclei, and takes its name from Ernest Rutherford’s famous explanation of alpha particle scattering from thin gold foil in 1911. The technique hinges around measuring the number and energy of ions scattered backwards from the sample surface after colliding with near-surface nuclei in the target material. The energy of the scattered ions will be dependent on their incident energy and on the mass of the sample atom which they hit, as well as the depth at which the collision interaction took

place. It is thus possible to determine the atomic mass and elemental concentrations of constituent atoms within a solid as a function of depth using this technique. Assuming conservation of momentum and kinetic energy, the *scattered projectile energy,* E_1 can be expressed as

$$E_1 = KE_o \quad \text{(a)}$$

and

$$K = \left(\frac{m_1 \cos\theta_1 \pm \sqrt{m_2^2 - m_1^2 (\sin\theta_1)^2}}{m_1 + m_2} \right)^2 \quad \text{(b)}$$

where, K is the ratio of the projectile energies called *Kinematic factor*. E_o, m_1, m_2 and θ_1 represents the energy of incident particle, mass of the incoming particle, mass of the target particle and scattering angle respectively. If $m_1 < m_2$, then plus sign is taken otherwise the minus sign is taken.

For a given θ_1, m_1 and E_o, the mass of the target atom determines the energy of the backscattered particles. So, in the case of a thin target, the energy spectrum shows several peaks corresponding to the mass of each element which constitute the target. While the above equation correctly determines the backscattered energies relative to measurement angle, it does not describe the angular distribution of the backscattering probability. For that we need the *differential cross-section of the backscattering* as given below:

$$\frac{d\omega}{d\Omega} = \left(\frac{Z_1 Z_2 e^2}{4E_o} \right)^2 \frac{1}{\sin^4\left(\frac{\theta_1}{2} \right)} \quad \text{(c)}$$

where, Z_1 and Z_2 indicate the atomic numbers of incident and target nuclei, respectively. The amount by which the incident ion energy is lowered after passing through a given distance is referred to as the *stopping power* of the material and is dependent on the electron distribution. This energy loss varies continuously with respect to distance traversed, so that stopping power is expressed as:

$$S(E) = -\frac{dE}{dx} \quad \text{(d)}$$

For high energy ions, stopping power is usually proportional to $\frac{Z_2}{E}$; however, precise calculation of stopping power is difficult to carry out with any accuracy. Ziegler and Chu [2] proposed semi-empirical tables of the stopping power values of the whole elements of the table of Mendeleev for particles of energies ranging between 0.4 and 4.0 MeV. With these tables, the stopping power makes it possible to determine the depth of the scattered atoms. Stopping power is generally expressed in units of eV/atoms/cm^2. So, by combining the scattering cross-section and stopping power, RBS allows calculating thin film composition and thickness.

Ion channeling is an ion scattering technique used for thin film analysis that takes the advantage of the material properties of single crystals. This technique is used to study crystal damage, defect concentration, epitaxial crystal alignment, etc. When an ion beam is aligned along a major crystal axis or

plane, ion-atom interaction probability is significantly reduced resulting in a large reduction of scattering events and deeper penetration of ions into the crystal. Simultaneously, redistribution of the ion flux in the channel occurs resulting in a phenomenon called *flux-peaking.* The ion flux is higher in the center of the channel than near the crystal axis or plane. Consequently, defects which are not located perfectly of the crystal lattice have a larger probability of scattering incoming ions. The combination of Rutherford backscattering and channeling (RBS/C) Spectrometry plays an important role in materials analysis of a variety of thin films as well as single crystal problems. So, I used this technique mainly to study the defects in ZnO single crystal.

In channeling measurements, a goniometer is used to position (tilt) the sample, such that the low index crystallographic directions of a crystalline target is aligned parallel to the incident beam. In this alignment mode, scattering usually occurs only from the first few monolayers of the target, and virtually no backscattering is recorded from within the target sample, since these atoms are shielded by the surface atoms. Thus a channeled RBS spectrum of a crystalline solid has a distinct surface peak, caused by scattering at the surface, followed by a very low background intensity for all other channels/energies. Conversely, a random spectrum, in which a crystalline sample is positioned such that no crystallographic directions are parallel to the beam, will produce a relatively uniform scattering intensity over all channels/energies. For samples

which contain a given amount of disorder, channeling the sample and comparing the resultant spectrum to that of a random spectrum or the channeled spectrum of a perfectly ordered crystal will give a quantitative measure of the extent of lattice disorder present. If the channeled spectrum matches that of the random spectrum, the crystal is usually thought to be amorphous at the depth where the two spectra coincide. The depth sensitivity of the RBS/C technique is particularly attractive when monitoring the depth and extent of lattice disorder within a sample.

RBS/C measurements presented in this thesis were made using the 1.7 MV tandem accelerator (NT 1700S, made by Nissin High Voltage Company) located in the Department of Electronic and Photonic Systems Engineering at Kochi University of Technology and a 2.5 MV Van de Graaff accelerator located in the Department of Power Engineering and Applied Physics at Hiroshima University, respectively. However the RBS/C beam line is equipped with a duoplasmatron ion source, and has a high-voltage tank with only one chain. A beam of 2MeV 4He+ ions was used in all cases to monitor the extent of lattice damage. The He beam was incident along the [0001] direction, and the backscattered beam was collected by Silicon surface barrier detector. RBS/C was conducted at RT in a vacuum chamber held at 10^{-6} Torr.

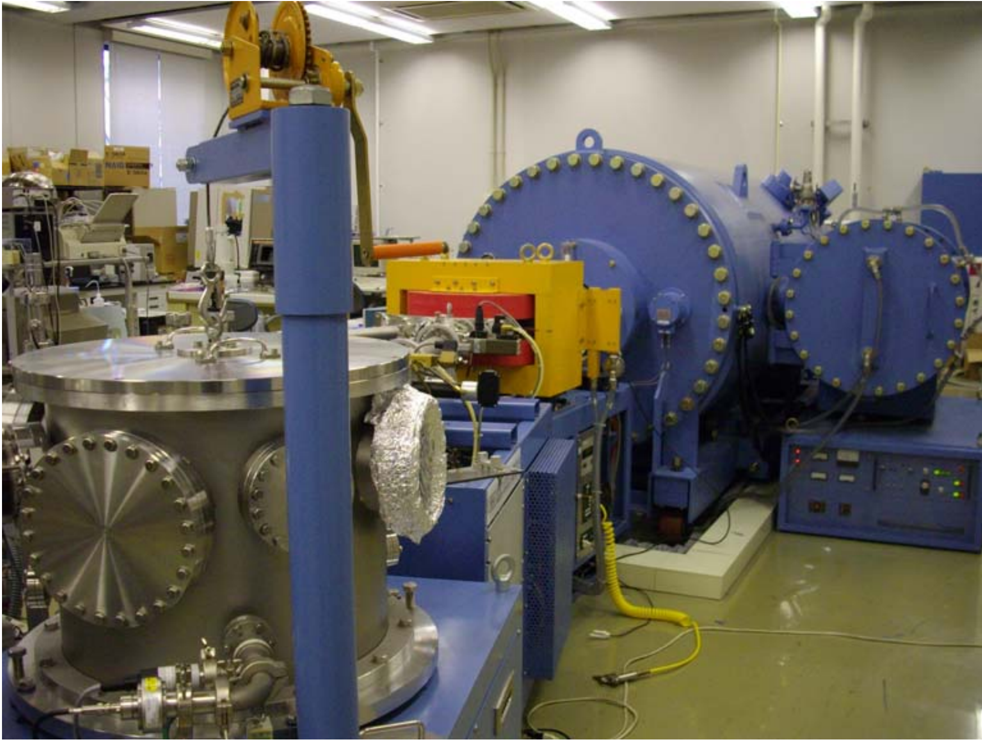

3.1 (a)

3.1 (b)

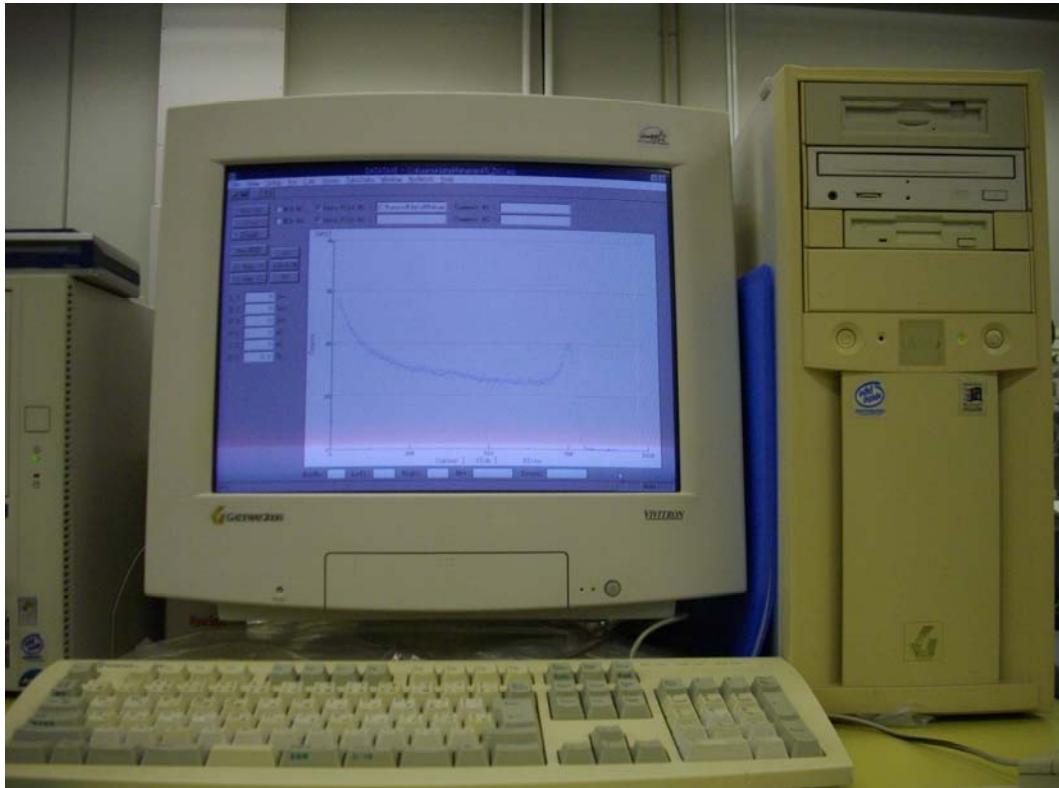

3.1 (c)

Figure3. (a) A 1.7 MV Nissin High Voltage Accelerator (NT 1700S) located in the Department of Electronic and Photonic Systems Engineering at KUT; (b) Multichannel Analyzer for processing RBS/C data; and (c) Computer panel for receiving data from multichannel analyzer.

3.2.2 Annealing

All annealing studies described in this thesis were conducted in air using rapid thermal annealing (RTA) system installed at KUT Research Institute.

3.2.3 Deposition

The deposition was done by vacuum deposition technique installed in the accelerator lab of Department of Electronic and Photonic Systems Engineering, Kochi University of Technology.

3.2.4 Atomic force microscopy

Atomic force microscopy (AFM) is a very innovative technique for measuring the surface morphology of materials with Angstrom-scale spatial resolution in ambient conditions, with essentially no sample preparation required. The principle of operation of an AFM is based around the interactions of a very small tip attached to a cantilever of known spring constant with a sample surface. By using a laser reflected from the end of the cantilever, minute deflections in the tip are detected by a position sensitive photodiode and converted to height or amplitude-of-displacement data. By scanning the tip across the surface of the sample, height scale or amplitude-mode images of the sample surface can be obtained. An AFM set-up is shown in figure 3.2.

AFM of semiconductor samples is conventionally carried out in one of two modes: contact mode AFM or tapping mode AFM. In contact mode AFM, the tip scans the sample in very close contact to the surface. The force on the tip is repulsive and usually set to a mean value of ～1 nN, as determined by pushing

Figure 3.2. SEIKO Nanopics 2100 AFM facility is shown here, installed in the Accelerator lab in the Department of Electronic and Photonic Systems Engineering at KUT.

the sample against the surface with a piezoelectric positioning element. As the tip is scanned across the sample surface, its deflection is monitored. A DC feedback amplifier is used to try and maintain a constant deflection value by sending a voltage to the piezoelectric scanner, causing it to raise or lower the sample relative to the tip. This voltage translates to a measure of the height of the sample surface features, and thus an image is created as a function of tip position as it is scanned across the sample. Contact mode AFM is the most common method of surface imaging, however for very soft samples such as

ZnO the applied force on the tip can damage the surface features. Even when using very small contact forces this can be an issue due to the presence of 10 - 30 monolayers of surface absorbed fluid (such as water vapour). The surface tension associated with this surface layer is sufficient to pull the tip down toward the surface, thereby causing damage and introducing artifacts into the image.

The second mode of AFM imaging, tapping mode, effectively minimizes this problem, overcoming the issues of friction, adhesion and electrostatic forces that can otherwise dominate contact mode imaging. Tapping mode involves lowering the tip until it comes into contact with the sample surface and then raising it again. It is achieved by using a piezoelectric crystal to oscillate the cantilever and tip at its resonant frequency. The oscillations are driven by a constant force, and the amplitude of oscillation is monitored. As the tip moves closer to the sample surface the oscillation amplitude is reduced. The tip height can thus be controlled through a feedback loop that responds to changes in the measured oscillation amplitude. By keeping a constant tip-sample separation through monitoring the amplitude and force to the tip, the surface of the sample is imaged as a function of cantilever oscillation. Aside from the reduced contact of the tip with the sample surface, the cantilevers in tapping mode AFM are much less susceptible to being pulled toward the sample surface by surface tension forces. Thus the use of much lower contact forces is

possible, limiting the impact of the tip on the surface. Commercially available Si cantilevers with force constants of 30 - 130 Nm^{-1} were used in all cases.

3.2.5 Hall-effect measurements

Four-point probe measurements are made using four identical probes, equally spaced along the surface of the sample. A current is forced through the outer two probes while measuring the voltage across the inner two probes. Using a high-impedance voltmeter or electrometer, very little current flows through the inner probes, minimizing the contact resistance associated with the voltage measurement. Using only two-point measurements, the voltage is measured with current-carrying probes. As such, the probe and contact resistances become non-trivial [3]. This technique is not error-free however, in the case of thin films. There are three correction factors that have to do with the geometry of the sample with respect to the probes. These factors compensate the measurement for proximity of the probes to an edge, lateral sample dimension and for sample thickness. Because of the small probe spacing used in the apparatus, probe placement with respect to the sample edge can be neglected [4]. Hall-effect measurements were conducted at KUT Research Institute using accent HL5500 Hall System.

However, the mobility of a semiconductor is important to know because it is a good indicator of crystal quality and electrical activity of dopants. Mobility can also degrade due to impurity scattering under very high dopant concentrations, but in this case is most likely to degrade from crystal damage and electrically inactive sites. Therefore, it is desirable to determine the true mobility of the sample, rather than assuming an intrinsic mobility for calculation purposes.

3.2.6 Luminescence

Luminescence measurements are useful for studying shallow impurities in electronic materials. These measurements consist of an excitation to generate carriers and a detection system to examine the luminescence emitted during de-excitation. There are many types of luminescence experiments including photoluminescence, cathodoluminescence, and electroluminescence differing largely in how carriers are excited in the material. The two forms utilized for these characterizations are photo- and cathodoluminescence.

Photoluminescence utilizes lasers (typically with photon energy greater than the bandgap) to optically excite carriers in a material. The photo-generated carriers can then recombine any number of ways, including photon emission. This optical recombination can be exploited to study the electronic states in a semiconductor by examining the emission spectrum. Methods for the detection of light include a spectrometer to disperse the light and either a solid-state

array (CCD or diode) or photomultiplier tube for higher sensitivity. Low temperature luminescence yields further information by removing thermally excited carriers, helping to resolve states occurring at similar energies. Temperature dependent data can also be used to determine the activation energy of states near the bandgap. In the PL measurements, a KIMMON Koha, 325nm HeCd laser was used for sample excitation and the luminescence was detected usingan Horiba Jobin Yvon, iHR320 spectrometer coupled with a thermoelectric cooled CCD.

3.2.7 Ion implantation

Ion implantation of materials is a very broad field with a range of applications in the field of semiconductor device processing. Detailed descriptions of the ion implantation technique and applications can be found extensively in literature. In this section, a brief description of ion implantation concepts as applicable to the experiments carried out in this thesis will be given.

Ion implantation typically involves the irradiation of samples with ions of different species and energy. Sources for implantation are very broad and include plasma as well as ion sources. The ions are accelerated from anywhere between a few 10's of kV to many MV, with the desired effect being to either include a new species into the sample (for example for doping purposes) or to create lattice defects in crystalline solids. When an energetic ion passes

through a solid, it undergoes collision interactions with the target nuclei and electrons. Nuclei collision interactions typically create displacements of the target atoms in the irradiated sample, producing lattice defects. The damage profile (both thickness of the damaged region and number of displacements occurring) within the irradiated sample will be dependent on the energy and mass of the incident ion, as well as other parameters such as binding energy, displacement energy and target density. Ion ranges and atomic displacements resulting from irradiation can be calculated. The Transport of Ions in Matter TRIM code is one such example of a software package that determines target displacement profiles and ion ranges from a Monte Carlo simulation of ballistic processes, based on statistical probabilities. Whilst this code is quite accurate for a simulated crystal in which no further interactions occur following irradiation, in reality, dynamic annealing processes are also present in real samples, particularly in ZnO which can undergo a large degree of dynamic annealing thus demonstrating its apparent radiation hardness [5]. Dynamic annealing involves the migration and interaction of implantation induced defects, in particular point defects, which can move through the crystal lattice and undergo annihilation. Dynamic annealing has been found to be heavily dependent on implant conditions such as ion mass, energy, dose, implantation temperature and beam flux [6] and is very difficult to simulate/model. Thus experimental studies on the effect of implantation conditions on damage profiles become essential for understanding and

predicting the impact of implantation-induced damage. Ion implantation was done from Nissin High Voltage Company.

3.3 References

[1] J. Nause and B. Nemeth, *Semicond. Sci. Tecnol.* **20,** S45 (2005).

[2] C. Boemare, T. Monteiro, M. J. Soares, J.G. Guilherme and E. Alves, *Physica B* **308-310,** 985 (2001).

[3] D. K. Schroder, *Semiconductor Material and Device Characterizations*, New York: Wiley-Interscience, 2-3 (1998).

[4] D. K. Schroder, *Semiconductor Material and Device Characterizations*, New York: Wiley-Interscience, 8-14 (1998).

[5] C. Coskun, D. C. Look, G. C. Farlow and J. R. Sizelove, *Semicond. Sci. Technol.* **19,** 752 (2004).

[6] J. S. Williams, *Mat. Sci. Eng., A* **253**, 8 (1998).

CHAPTER 4

Metallic contact to ZnO

4.1 Introduction

Metallic contacts with compound semiconductors of group A^{II} and B^{VI} have a great importance for investigation of the various surface properties of these compounds and to evaluate the possibility of fabricating devices based on these semiconductors having unique conductivity and generally interesting properties [1]. The most interesting of these compounds is ZnO because of its many possible applications [2-12].

Metal contacts to semiconductor surfaces usually fall under two categories, Ohmic or Schottky, depending on their characteristics. An Ohmic contact is defined as one in which current may be passed through in both directions, with a negligible voltage drop. Additionally, it should not change the nature of the device. A Schottky contact on the other hand is a rectifying contact; that is one which allows current to flow through the device in one direction only, due to the formation of a potential barrier at the metal-semiconductor interface caused by a difference in the work function of the two materials.

It is important to realize an Ohmic contact for long-lifetime operation of optical and electrical devices. If the high contact resistance exists between metal and semiconductor then device performance might be degraded severely due to metal stress or contact failure. In order to obtain high performance ZnO

based optical and electrical devices, it is necessary to achieve Ohmic contacts having low resistance and thermally stable as well as reliable. This can be achieved either by performing surface preparation to reduce metal-semiconductor barrier height which could allow an increase in carrier tunneling probability or by increasing the effective carrier concentration on the surface perhaps taking the advantage of oxygen loss [13]. Ohmic contact metallization should be one of the main targets for improving device performance which plays an important role in device technology.

Transition metals on zinc oxide are often studied as model catalysts and as growth substrates for metals. The oxidation state of Ti on ZnO depends highly on the total Ti coverage. At low coverage the Ti oxidizes completely and at high coverage a metallic Zn component exists in the deposit indicating that the Ti-layer reduces the substrate [14]. The Gibbs free energy of formation for TiO is much lower than that for ZnO [15]. Metal/ZnO contacts, including ohmic and Schottky types, play an important role in device performance and better thermal stability are expected for metal Ohmic contact to wide band gap semiconductors.

The influence of the stress state of the Ti layers in stable systems has been reported but there are few studies on the role of this metal in instable or reactive interfaces. Ti was chosen as it has better adhesive force than other metals to the ZnO surface, an attempt has been taken aiming to study the

Ti/ZnO interface stability as a function of annealing temperature by means of Rutherford Backscattering Spectrometry and Channeling technique which will be presented in this chapter. As Ti is more electropositive than Zn, a reaction at the interface during deposition can be expected. The reaction kinetics during and after deposition and atomic composition at the interface of Ti with ZnO is discussed as a function of annealing temperature.

4.2 Experimental Methods

High quality wurtzite Zn face [0001] ZnO single crystals were purchased from MTI Co., USA. Ti thin film of 16 nm thickness was developed on the ZnO substrate by using vacuum deposition technique. Following deposition, the ZnO single crystal was divided in three smaller samples, one of them was as-grown sample and the other two samples were annealed in air at 300 $^{\circ}$C and 400 $^{\circ}$C for 15 minutes, respectively. Crystalline quality and interface stability were investigated by means of the Rutherford Backscattering Spectrometry and Channeling techniques, for which 1 mm collimated 2 MeV $^{4}He^{+}$ beam was used. The targets were mounted in a computer controlled two-axis goniometer arrangement. The backscattered particles were detected with Si surface barrier detector placed at 168° (Figure 4.1) with respect to the beam direction having an energy resolution of ~20 keV to evaluate the crystalline quality.

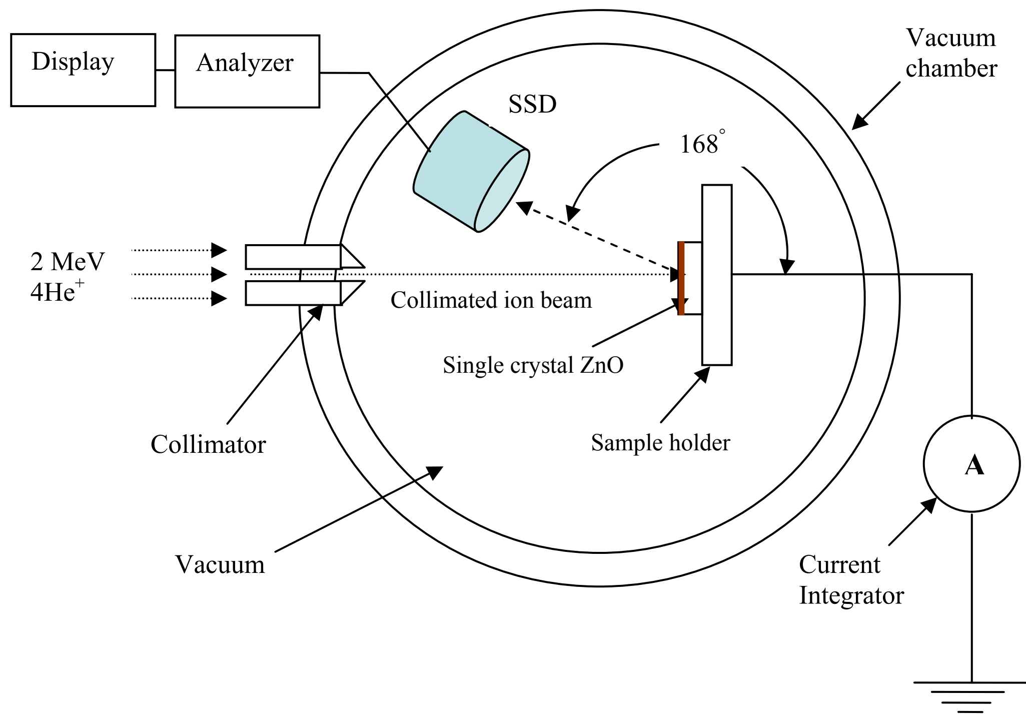

Figure 4.1. Experimental setup for evaluation of crystalline quality after deposition. Ti was deposited on the Zn face (0001) single crystal ZnO. Silicon surface barrier detector has been placed at 168° to collect backscattered ions.

To study the interface stability, the scattered particles were collected by the glancing angle detector placed at 100° as shown in Figure 4.2. This type of placement of the detector has no influence on the close-encounter interactions and channeling of the incident beam but does affect the relation between detected energy widths and depth intervals. At grazing exit angles, the

outgoing path length of the emergent particles may have five times that for the path length of laboratory arrangement (~170°) scattering [16] as shown in Figure 4.1.

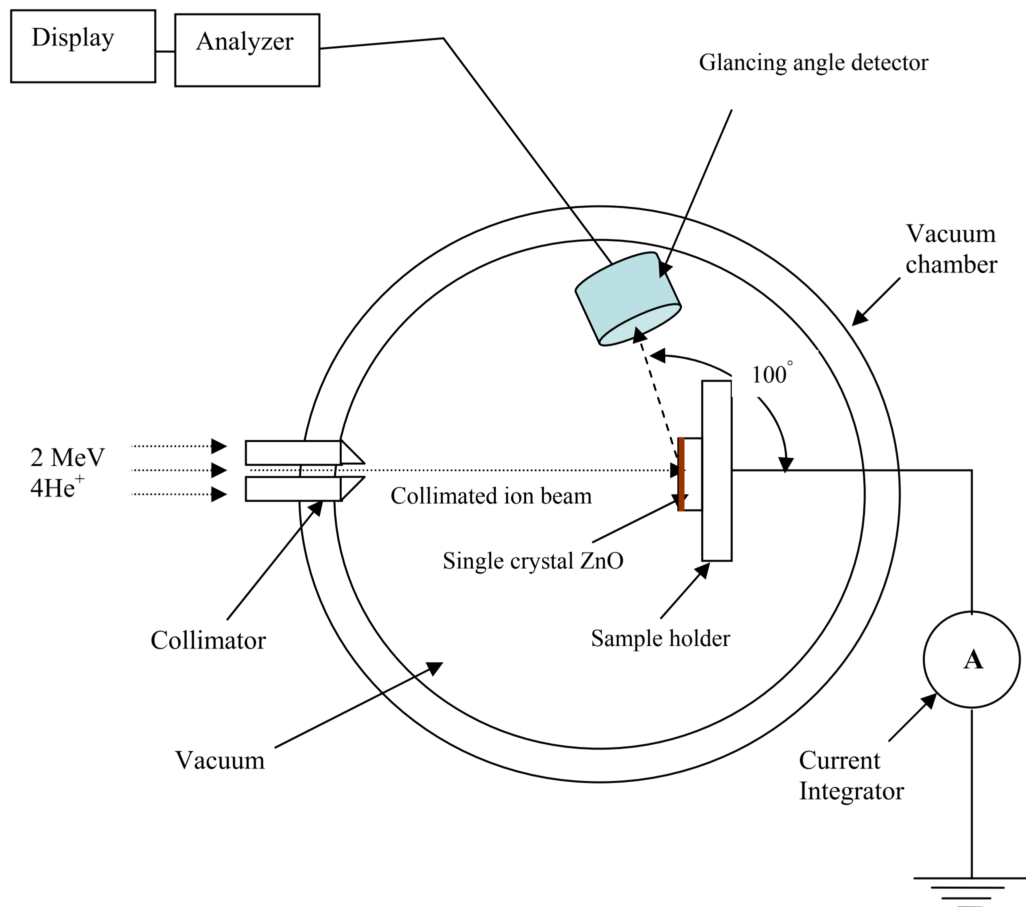

Figure 4.2. Experimental arrangement for studying Ti/ZnO interface stability. Glancing angle detector has been placed at 100° to collect back-scattered He ions from the interface.

However, the stretching of the depth scale spreads the total number of detected scattering events in a given thickness over greater energy interval and hence decreases the number of counts per energy channel in the bulk crystal.

4.3 Results and discussion

Figure 4.3 shows the RBS/C spectra of a virgin bulk ZnO single crystal. In this case, Si surface barrier detector was placed to collect backscattered particle at angle 168° with respect to the injected $^{4}He^{+}$ ion beam direction. The percentage ratio of channeling yield to random yield is called minimum yield, χ_{min} which indicates the crystalline quality. However, the minimum yield for this virgin sample was only 2% which suggests that it has good crystallinity and purity. The surface edge of Zn and O can be seen from this figure.

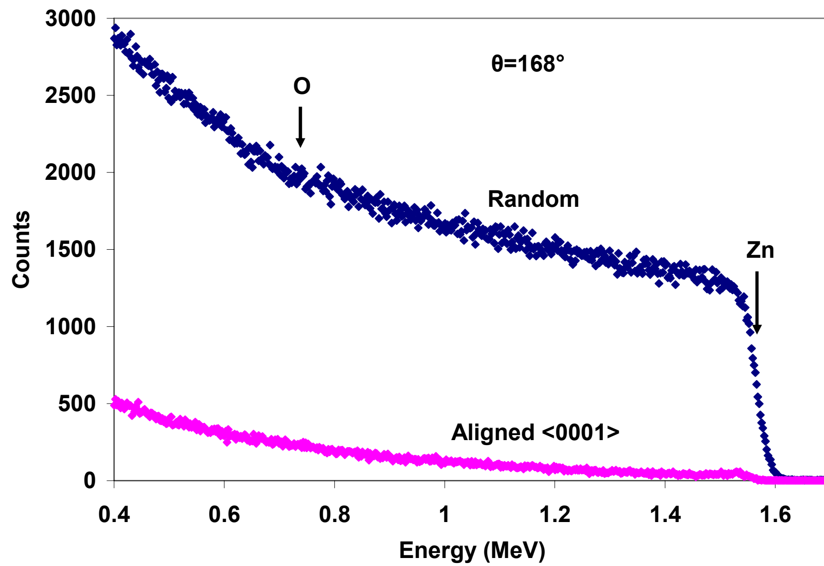

Figure 4.3. RBS/C spectra of Zn face (0001) oriented virgin single crystal ZnO. The surface edge of Zn and O can be seen from this figure and the reduced aligned signal indicates no defect observed on its passage during ion channeling.

Figure 4.4 shows the random and <0001> aligned RBS spectra for the Ti deposited single crystal ZnO sample. The surface edge for the different elements (O, Ti and Zn) can be observed here without any deposition effect.

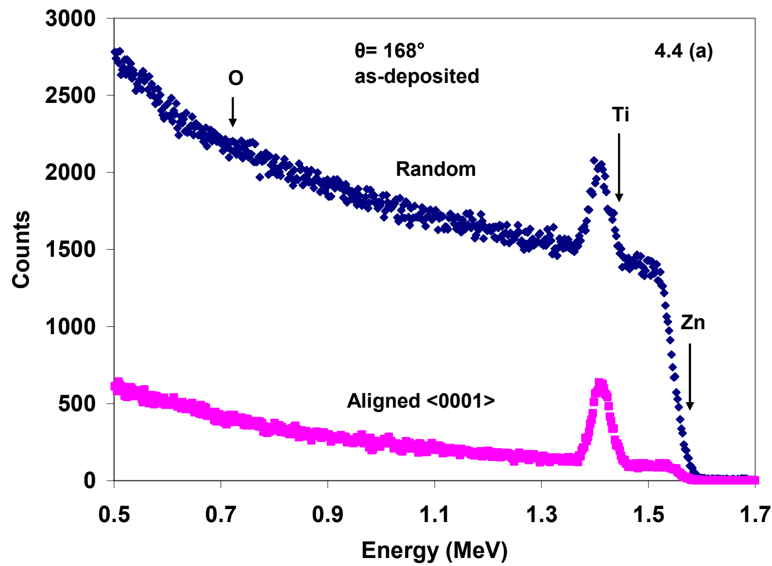

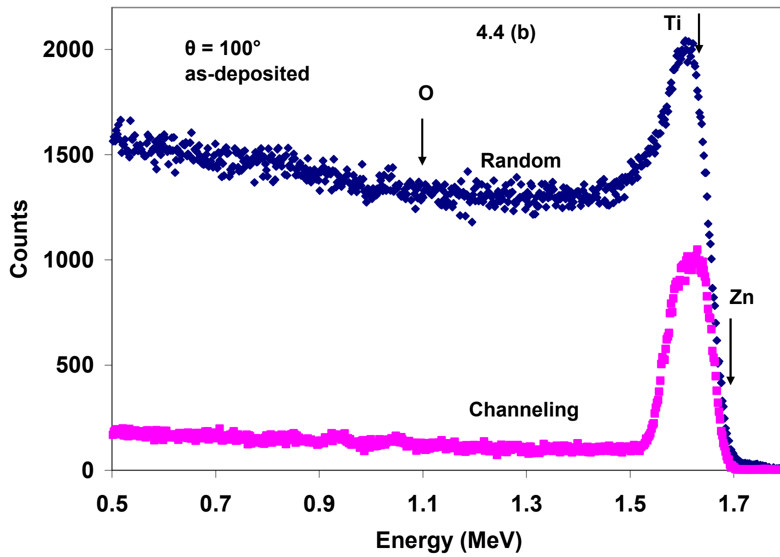

Figure 4.4. (a) RBS/C spectra of Ti/ZnO sample while backscattered detector was placed at 168° to evaluate crystalline quality; (b) RBS/C spectra of (0001) oriented single crystal ZnO after Ti deposition. The backscattered ions were collected using glancing angle detector placed at 100° to improve surface sensitivity.

The reduced Zn signal in the channeling spectrum, when compared with random acquisition yield, indicates that the as-deposited sample is below the amorphisation threshold [17]. For this sample the minimum yield, (χ_{min}), increased to 7% from the substrate ZnO which was calculated from the spectra measured by the SSD placed at 168°. This value of χ_{min} is quite large for simply deposited sample as compared with that one of 2% for the virgin single crystalline ZnO, which implies that severe damages occurred by deposition with interface reaction between Ti and ZnO even at room temperature.

Figure 4.5 shows the RBS/C spectrum of the Ti/ZnO sample after annealing at 300°. In this spectrum a new peak appeared more clearly due to surface oxygen. As-deposited sample also has surface oxygen because the sample was exposed in the air after deposition. After annealing Ti layer was oxidized more extensively, so the oxygen signal became stronger than that of as-deposited one. In this case, the minimum yield from the substrate ZnO single crystal was found of 16%, which indicates that the crystalline quality becomes degraded very much after annealing at 300 $^{\circ}$C.

It has been reported by Soo Young Kim et al. [18] that a new peak for TiO or TiO_2 was observed in XRD experiment due to annealing effect at 300 $^{\circ}$C. From thermodynamic data of changing of the Gibbs free-energy per mole of oxygen [15] implies that TiO has a more stable phase than TiO_2 at all temperatures

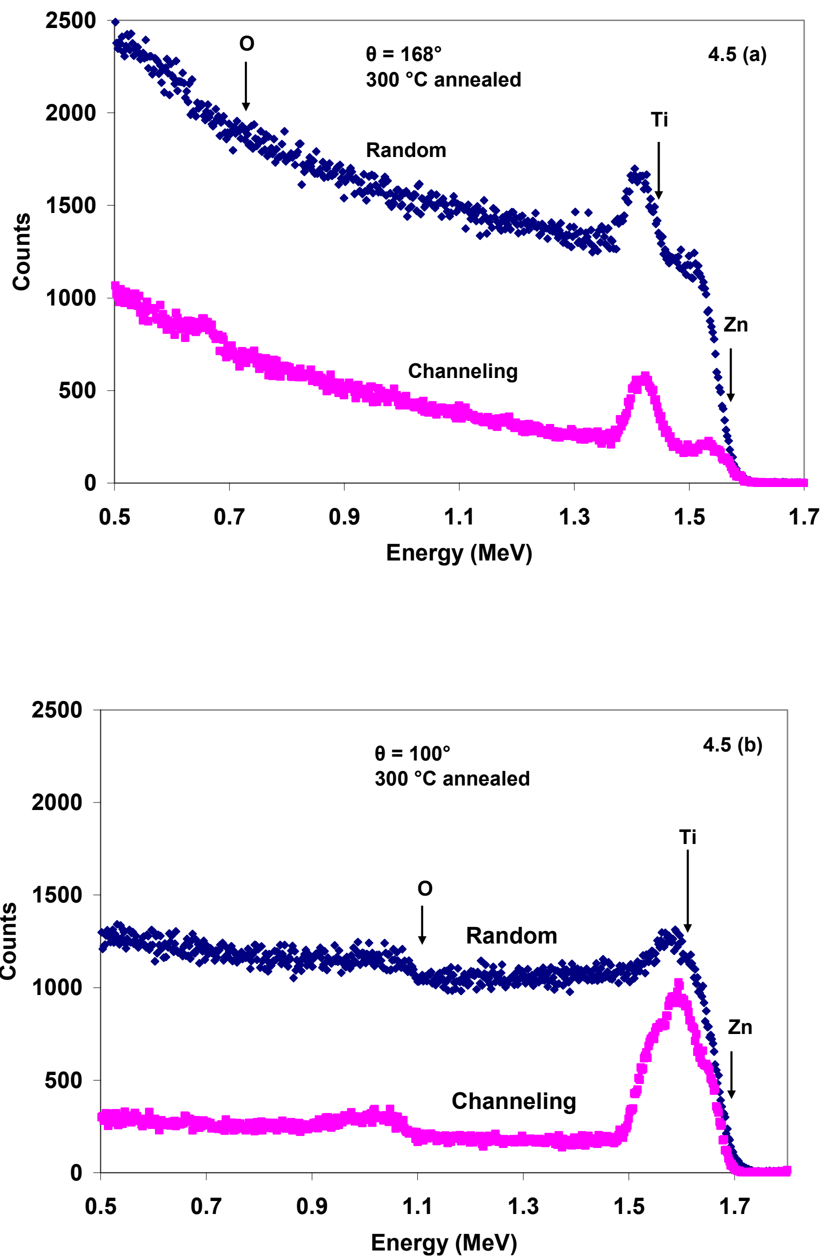

Figure 4.5. (a) RBS/C spectra obtained from backscattering detector placed at 168° for the Ti deposited ZnO sample after annealing at 300 °C; (b) RBS/C spectra of the same ZnO single crystal sample with glancing angle detector (100°). In this case, Ti peak becomes wider than that of as-deposited sample.

which means oxygen atoms in substrate ZnO reacts with the Ti layer to form TiO. The peaks in Fig. 4.5 became wider as compared with Fig. 4.4, suggests that Ti diffuses towards the bulk due to interfacial reaction.

In Figure 4.6 we show the RBS/C spectra obtained for a polycrystalline Ti film deposited on single crystal ZnO sample annealed at 400 °C. In this spectra Ti peak was overlapped because it does not affect the channeling as a polycrystalline material or due to flux-peaking effect of ion channeling. For this sample the minimum yield was found to be 10% which is less than that for the sample annealed at 300 °C but greater than as-deposited one.

A diffused Zn peak was clearly observed in figure 4.6 which indicates that a significant amount of Zn had moved on the surface after post annealing at 400 °C. The calculated value of diffused Zn was approximately 6.4 Ч 10^{16} atoms/cm^2. This diffusion may be happened due to some crack onto the surface, even there are no cracks diffusion can arise. However, it has been reported by another group of researchers [15] that the O-Ti bond increases with an increasing annealing temperature, meaning the possibility for formation of TiO at the interfacial region.

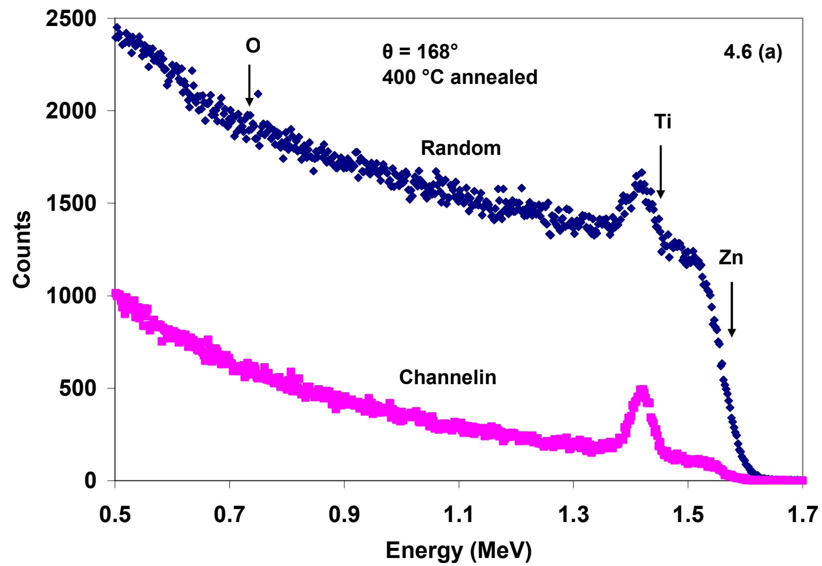

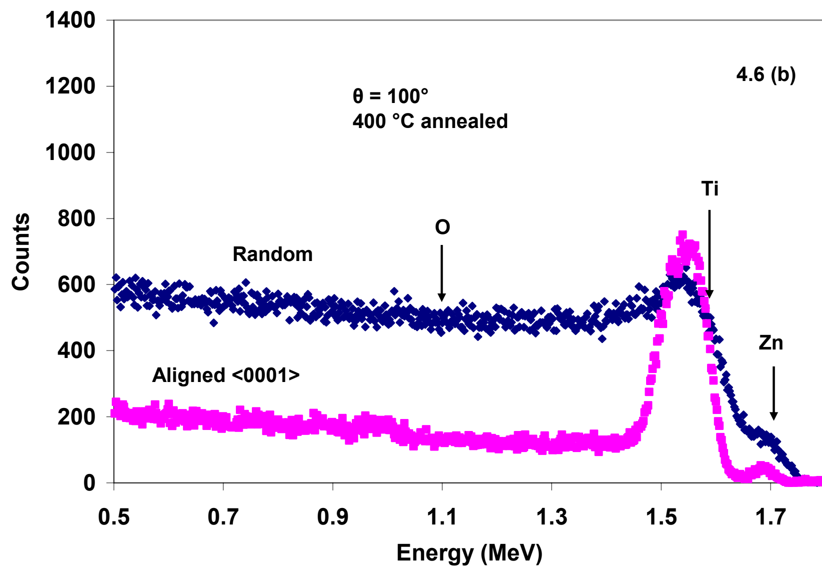

Figure 4.6. (a) RBS/C spectra obtained from backscattered detector placed at 168° for the sample after post-annealing at 400 °C; (b) RBS/C spectra of the same Ti/ZnO sample collected by grazing exit angle detector (100°). In this case, Ti peak becomes overlapped due to so called flux-peaking effect of ion channeling.

Since Ti has a stronger tendency to react with O than Zn, it is natural that Ti reacts with substrate oxygen leaving free Zn atoms behind, and those easily migrate onto the surface. The reaction kinetics at the interface region of Ti/ZnO can be explained with the following proposed model Fig. 4.7. The oxygen atoms in ZnO substrate react with Ti layer to form TiO and leave free Zn atoms behind. Since the samples were annealed in the air atmosphere, it will become stable forming TiO_2 in the interfacial region and free Zn atoms will be available onto the surface which reacts with oxygen in the air to form ZnO.

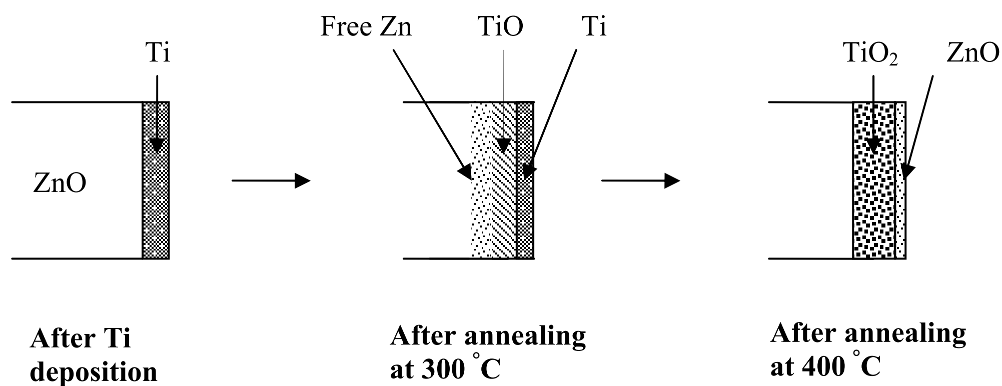

Figure 4.7. Possible reaction mechanism of Ti/ZnO interfacial region.

Surface morphology of as-deposited and annealed Ti/ZnO samples was investigated by means of Atomic Force Microscopy as shown in Fig. 4.8. There were no cracks in the AFM images after deposition and annealing except very few dust or scratches. It suggests that Zn atoms were moved onto the surface due to diffusion which supports the above explanation.

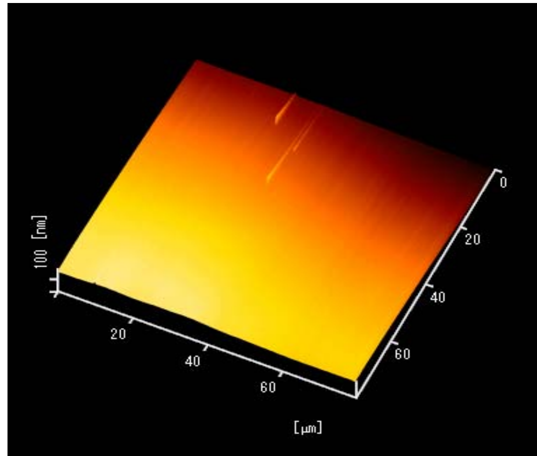

Figure 4.8. (a). AFM image of Ti deposited ZnO single crystal. Some scratches may exist here on the surface.

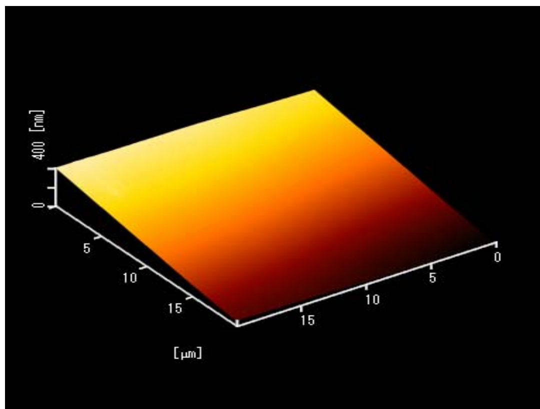

Figure 4.8. (b). AFM image of Ti deposited ZnO single crystal after annealing at 300 °C. Smooth surface is observed here.

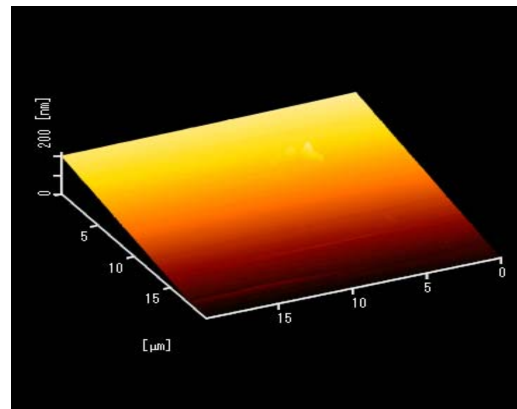

Figure 4.8. (c). AFM image of Ti deposited ZnO single crystal after post-annealing at 400 °C. Little dust may exist here on the surface.

4.4 Conclusion

After Ti deposition the value of normalized yield from substrate ZnO became 7% whereas it was only 2% for virgin single crystal ZnO. After annealing the sample at 300 $^{\circ}$C, this value increased as much as 16% but it was reduced to 10% after post-annealing at 400 $^{\circ}$C. After annealing at 300 $^{\circ}$C, oxygen atoms might be out-diffused from ZnO and as a result it could produced oxygen vacancies, $V_{o,}$ at the interface region. Since TiO is more stable than ZnO, there is a possibility for oxygen atoms in ZnO substrate to react with Ti layer to form TiO while the sample was annealed at 300 $^{\circ}$C. From our RBS study, it was found that Ti peaks becomes wider with increasing temperature which indicates that Ti layer reduces the substrate that is well agreed with the report by another authors [14]. It has been reported by Kim *et. al* [19] that metals such as Al and Ti can form good and stable Ohmic contacts to a ZnO surface but there is an inconsistency in our study, as a significant amount of Zn (approximately 6.4 Ч 10^{16} atoms/cm^2) moved onto the surface due to diffusion after post-annealing the sample at 400 $^{\circ}$C which could lead to the degradation of the device with this contact metallization.

4.5 References

[1] S. A. Medvedev, ed., *Physics and Chemistry of A^{II} B^{VI} Compounds [Russian translation],* Mir, Moscow (1970).

[2] R.E.I. Schropp, A. Madan, *J. Appl. Phys.* 66 (5) (1989), 2027-2031.

[3] R. G. Heideman, P. V. Lambeck, J. G. E. Gardeniers, *Opt. Mater.* 4 (6) (1995), 741.

[4] M. Penza, C. Martucci, V. I. Anisimkin, L. Vasanelli, *Mater. Sci. Forum.* 203 (1996), 137.

[5] M. G. C. Hutchins, *Energy and Environment,* Pergamon, Oxford, 3 (1990), 1398.

[6] M. Purica, E. Budianu, E. Rusu, *Microelectron. Eng.* 51-52 (1-4) (2000), 425.

[7] M. Huang, S. Mao, H. Feick, H. Yan, Y. Wu, H. Kind, E. Weber, R. Russo, P. Yang, *Science* 292 (2001), 1897.

[8] B. Sang, A. Yamada, M. Konagai, *Jpn. J. Appl. Phys.* 37 (2B) (1998), L206.

[9] A. Ohmoto, M. Kawasaki, *IEICE Trans. Electron.* E83-C (10), (2000), 1614.

[10] N. W. Emanetoglu, C. Gorla, Y. Liu, S. Liang, Y. Lu, *Mater. Sci Semicond.*

Proc. 2 (1999), 247.

[11] F. J. Von Pressing, H. Jeng, E. S. Kim, *Smart Mater. Struct.* 7 (1998), 396.

[12] P. M. Martin, M. S. Good, J. W. Johnson, G. J. Posakony, L. J. Bond, S. L. Crawford, *Thin Solid Films* 379 (2000), 253.

[13] J. H. Lim and S. J. Park, *Zinc Oxide Bulk, Thin Films and Nanostructures: Processing, Properties and Applications,* 267-283 (2006).

[14] Oral Abstract Presentation in France, (2006).

[15] I. Barin, F. Sauret, E. S. Rohnhof, W. S. Sheng, *Thermochemical Data of Pure Substances* (New York: VCH, 1989).

[16] L. C Feldman and J. W. Mayer, *Fundamentals of Surface and Thin Film Analysis,* Elsevier Science Publishing Co., Inc. 120 (1986).

[17] T. Monterio, M. J. Soares, A. Neves, M. Oliveira, E. Rita, U. Wahl, E. Alves, *Phys. Stat. Sol.* 1 (2) (2004), 255.

[18] S. Y. Kim, H. W. Jang, J. K. Kim, C. M. Jeon, W. I. Park, G. C. Yi, J. L. Lee, *J. Electronic Materials* 31 (2) (2002), 869-870.

[19] H. K. Kim, S. H. Han, T. Y Seong and W. K. Choi, *Appl. Phys. Lett.* **77**, 1647 (2000).

CHAPTER 5

Influence of ion current density on damage buildup in ZnO

5.1 Introduction

Ion implantation of semiconductors is widely used in the microelectronics industry for selective area doping and electrical isolation of devices [1, 2]. It is an attractive technique for such purposes for a number of reasons. With masking, only selected areas of the device will be subject to implantation, allowing for an increase in the functionality of devices on a single chip. This limits the need for delicate and time consuming selective area etching and re-growth. Implantation can also be conducted on a large scale and is a relatively economically viable process. Given the current status of the field, ZnO devices will soon become a commercial reality, and thus there is increasing need for a detailed understanding of potential processing techniques for this materials system. Furthermore, given the high predicted value of the Curie temperature (T_C) for ZnO, ion implantation will also be applicable for the creation of dilute magnetic semiconductors based on ZnO [3].

Frequently hailed for its radiation hardness [4], ZnO would appear to be a perfect candidate for *p*-type doping by ion implantation. In order for large scale doping to be feasible in this material system however, a thorough understanding of damage accumulation and its recovery of implantation-produced defects in ZnO is imperative [5]. In this chapter, the role of implantation ion current density on damage formation in ZnO has been studied. This was achieved through a combination of RBS/C spectrometry.

5.2 Previous studies

Whilst there are extensive reports of ion-implantation studies of ZnO in the literature [5, 6, 7, 8, 9] there are very few that focus on the recovery of implanted ZnO by annealing [10–14]. Of these studies, however, none directly with the re-crystallization of heavily-damaged ZnO at high temperatures. Jeong *et. al.* [11] recently presented an annealing study of low-energy As+ implants into ZnO at RT involving relatively low doses (10^{15} cm^{-2}). They annealed their samples at various temperatures and reported that an anneal at 800 ◦C for 1 hour produced an optimum recovery of crystallinity [11]. Chen et. al. [13] conducted phosphorous implantation into ZnO at low doses (10^{13} - 10^{15} cm^{-2}) and examined the defect recovery in this system. Their study revealed that ion implantation resulted in the formation of oxygen vacancy clusters which agglomerated with increasing annealing temperature. These clusters were then observed to be annealed out at 1100 ◦C. Recent studies on ion implantation of potential *p*-type dopants such as arsenic [12, 15] and nitrogen [16] into ZnO are showing promise as a viable method of achieving *p*-type conductivity in ZnO. Indeed, As has been predicted to be one of the best candidates for *p*-type doping in ZnO as a result of size-effects, promoting acceptor-related impurity states in ZnO [17, 18]. However, it was decided that the large mass of the In ion would promote the creation of damage within the ZnO lattice, allowing highly defective layers to be achieved at doses lower than that for implantation with a lighter ion.

ZnO is a II-VI semiconductor material with a wide wide-band-gap ($E_g \sim 3.37$ eV at room temperature) and an exciton binding energy of 60 meV [19]. It has potential technological applications in both short-wavelength light-emitting devices and semiconductor spin electronics [20-22]. Besides these unique optical and electrical properties, it was shown by irradiations with electrons [23-26], protons [27,28] and heavier ions [29,30] that ZnO is significantly more radiation resistant than other semiconductors including GaN (its major rival regarding electronic and optoelectronic applications and a compound semiconductor with similar structural properties). Ion implantation was used to dope single crystalline ZnO with optically [30], electrically [31,32], or magnetically [33] active ions. Ion implantation is a powerful tool for introducing controllable ion concentrations at precise depths below the surface with the facility of selective area doping; however, it produces lattice damage and hence the processes of damage build-up and recovery need to be understood [34].

At present, there are still serious challenges to overcome in processing ZnO, including electrical doping, metallization and electrical isolation. In particular, p-type doping of ZnO is rather challenging due to the complex behavior of intrinsic lattice defects in this material. The problem with doping by ion implantation is obviously related to dopant activation efficiency and unwanted effects of ion-beam-produced lattice defects on the electrical properties of the

material. An understanding of ion-beam-damage processes in ZnO can be achieved through detailed studies and it is desirable to understand the potentiality of ion implantation as a device processing tool. For our study, as a donor Indium ions were used to dope electrically into single crystal ZnO by ion implantation to investigate the damage profile of single crystal ZnO as a function of implantation ion current density and thermal treatment.

5.3 Experimental methods

Single crystal bulk wurtzite ZnO samples used in this study were purchased from MTI Co., USA. As specified by the grower, the samples were nominally undoped, (0001) oriented, single side (Zn-face) polished. The dimension of each crystal was 10 mm Ч 10 mm Ч 0.5 mm. Implantation of In^+ ions under a same acceleration voltage of 120 keV was done at room temperature to a same dose of 1Ч10^{15} cm^{-2} with different ion current densities of 0.7 and 1.4 $\mu A.cm^{-2}$, respectively. During implantation, samples were tilted by 7° relative to the incident ion beam to minimize channeling.

A post-implantation annealing is needed to electrically activate the dopant species and to remove the crystal defects due to ion bombardment. To study the damage build-up by implantation and its behavior under different annealing conditions after implantation, the ZnO single crystal was divided into four

smaller samples, one of them was an as-implanted sample and the other three samples were annealed at 600 °C, 800 °C and 1000 °C, respectively, in oxidizing atmosphere for 60 minutes. Crystalline quality, damage recovery and the influence of implantation ion current density on defects accumulation in the bulk ZnO were studied by means of Rutherford Backscattering Spectrometry and Channeling techniques (RBS/C).

RBS/C measurements were performed using the 2.5 MV Van de Graaff-type accelerator located at Hiroshima University, Japan. The separation of peaks corresponding to consecutive elements leads to the use of relatively heavy particles for backscattering was detected at large angle θ. The energy value of the incident particles is the result of a compromise: the scattering cross section decreases with increasing incident energy while the resolving power increases. From theses considerations, we finally used a collimated 2 MeV $^4He^+$ ion beam and silicon surface barrier detector with a resolution of 15 keV placed at 165° was used to collect the backscattering particles. The ionic current is around 10 nA. The diameter of the $^4He^+$ ion beams is typically 2 mm. The signal was recorded through a low capacitance charge amplifier. Moreover, in order to prevent channeling conditions, the samples were tilted by 5° with the normal during RBS measurements. The samples were aligned to the crystal axis <0001> to investigate the crystal defects. The pressure inside the vacuum chamber during the experiments was about 10^{-7} mbar. The peak depth of

Indium was typically 32 nm, calculation performed by simulation software SRIM 2006.

5.4 Results and discussion

The main feature of this study is to investigate the damage buildup behavior as a function of implantation ion current density. Figure 5.1 shows the random and <0001> aligned RBS spectra for the virgin single crystal ZnO. The surface edge of substrate oxygen and Zn can be observed here. The reduced Zn signal in the channeling spectrum, when compared with random acquisition yield, indicates the excellent crystalline quality of the bulk ZnO. For this un-implanted single crystalline ZnO, the minimum yield (χ_{min}) is only 2.0 %.

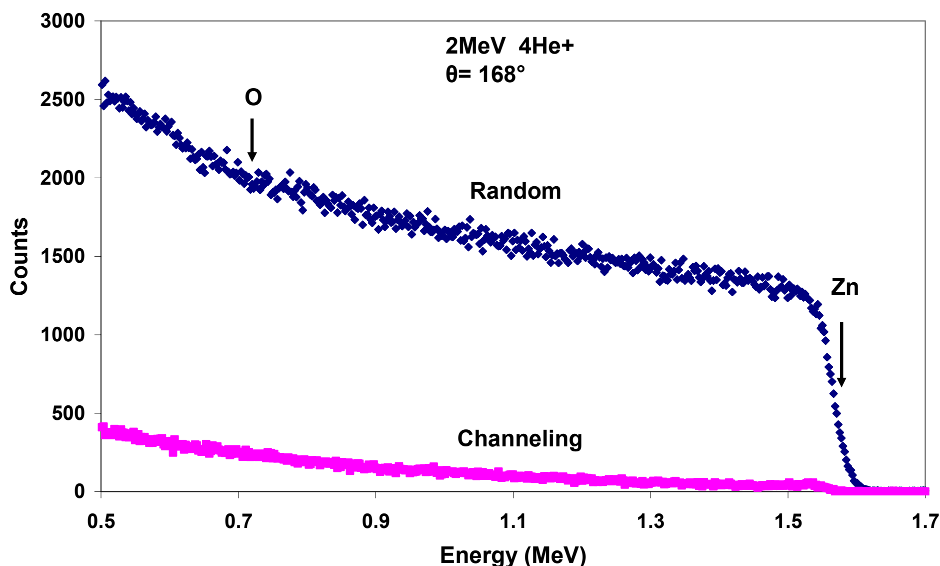

Figure 5.1. Comparison of RBS and channeling spectra of virgin single crystal ZnO with one side polished (Zn- face).

Figure 5.2 shows the RBS and <0001> aligned spectra of In^+ implanted single crystal ZnO with ion current density 0.7 μA/cm^2. As a measure of damage concentration, the minimum yield χ_{min} was calculated within a window which can evaluate the crystalline quality with different treatments such as by ion implantation, deposition and annealing. To calculate the damage level created by In^+ ion implantation, the yields of the aligned spectrum comprising the whole implanted layer were integrated as indicated in Fig. 5.2. In this figure, the minimum yield, χ_{min} was calculated from that window to be as large as 18% which indicates that damage was produced in the implanted layer cause degradation of crystalline quality of the bulk ZnO after In^+ implantation. Damage shoulder is clearly observed in Fig. 5.2, which is not appeared in the case virgin crystal as shown in Fig. 5.1. The integrated intensity of damage shoulder was calculated to consist of 37,500 ± 200 counts.

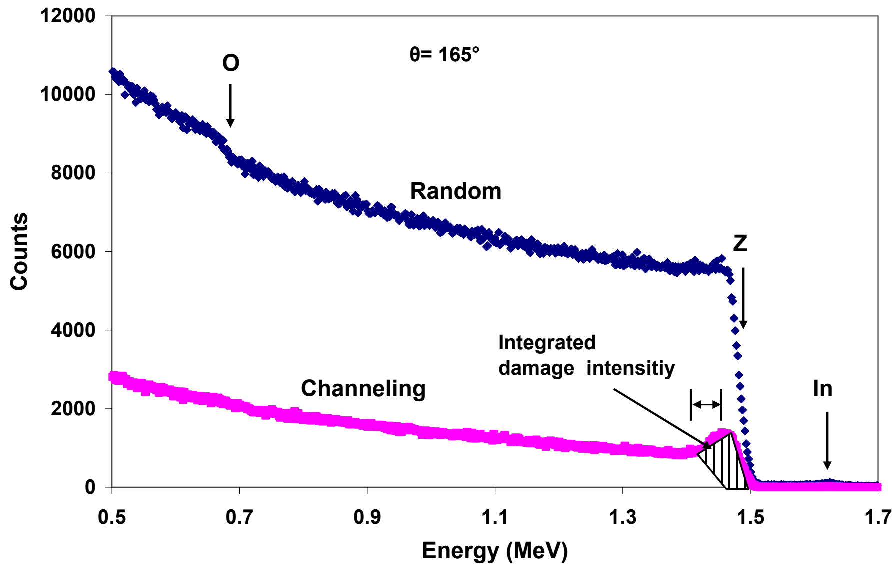

Figure 5.2. RBS and channeling spectra of ZnO single crystal after In^{+} implantation at a fluence of 1Ч10^{15} ions/cm^2 with ion current density 0.7 μA/cm^2. The implantation was done at room temperature under an acceleration voltage of 120 keV.

From their structural and post-implantation annealing studies of Fe^{+} implanted (at room temperature with 100 keV, at a fluence of 1Ч10^{16} ions/cm^2) high quality ZnO single crystals, Monteiro *et al.* [35] reported that disorder increased the χ_{min} from 2% to 50%.

However, the implanted atom comes to rest ~ 33 nm below the surface in a region of disorder created by its passage. The electrical properties of the implanted layer depend on the lattice position of the impurity and the amount of lattice disorder. In our study, we assumed that single ion strikes on the

surface and excites 1 μm^2 (10^{-8} cm^2) area resulting damage buildup in the single crystal. Then the fluence of In^+ ions while the implantation ion current density was 0.7 μA/cm^2, can be calculated as follows.

$$0.7\ \mu\text{A/cm}^2 = 0.7 \times 10^{-6} \times \frac{1}{1.6 \times 10^{-19}} ions/cm^2.\text{sec} \approx 4.4 \times 10^{12} ions/cm^2.\text{sec}$$

Then the total number of ions per μm^2 of the surface is, $4.4 \times 10^4 ions/\mu m^2.\text{sec}$.

Therefore, the mean duration between one collision and the next is $\frac{1}{4.4 \times 10^4} \approx 2.3 \times 10^{-5}$ sec. The integrated intensity of damage shoulder was calculated to consist of 37,500 ± 200 counts.

Figure 5.3 shows the spectra of yields in random direction as well as channeling direction for In^+ implanted single crystal ZnO with an implantation ion current density of 1.4 μA/cm^2. In this case, the damage raised the minimum yield χ_{min} from 2% to 22% which is greater than that for lower ion current density. It suggests that crystalline quality also became worse than in the previous case (Fig. 5.2) and damage buildup in ZnO single crystal increased as a result of increasing ion current density during implantation. A similar effect on ion current density has been reported by Battistig *et al.* [36] for the case of another wide band-gap semiconductor, SiC. In our study, for an ion current density of 1.4 μA/cm^2, the integrated damage peak intensity was higher (43,900 ± 350 counts) than that which occurred with lower ion current density of 0.7 μA/cm^2.

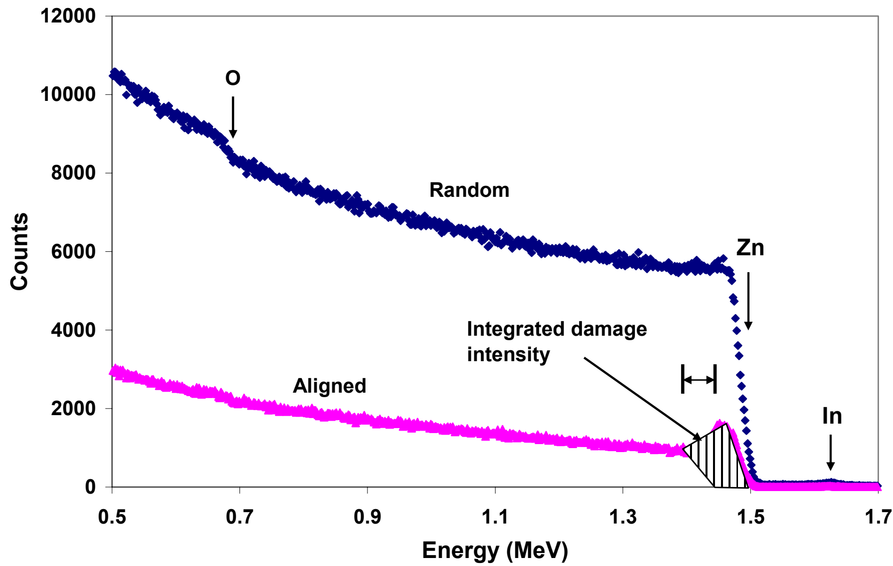

Figure 5.3. RBS and <0001> aligned spectra of single crystal ZnO after In^+ implantation with a dose of 1×10^{15} ions/cm^2. In this case, implantation ion current density is 1.4 μA/cm^2.

The duration of excitation by single In^+ ion calculated in the same manner was also higher while the current density was 1.4 μA/cm^2. Doing similar calculation we know that the mean duration of ion arrivals is 4.6×10^{-5} sec in this case. This indicates that the level of bulk disorder gradually increases as a result of increasing ion current density. Damage enhancement due to increase of the ion current density should arise in the wake of re-excitation by the second ion of the excited area by the first ion. From these considerations, we can conclude that the excitation life-time in our case is in the order of 10^{-5} sec.

The RBS and channeling spectra of the damaged region in the substrate ZnO are illustrated in Figure 5.4. The trend of disorder accumulation is clearly

visible here. The thickness of the damaged layer was reduced due to annealing indicating that some re-crystallization might have occurred near to the implanted/non-implanted interface. A similar feature has been explained by Battistig *et al.* [36] with Al implantation in SiC. They also mentioned that higher ion current density amorphises the surface of the sample and damaged layer is situated in the middle of the amorphous layer, suggesting that re-crystallization started from the substrate as well as from the surface.

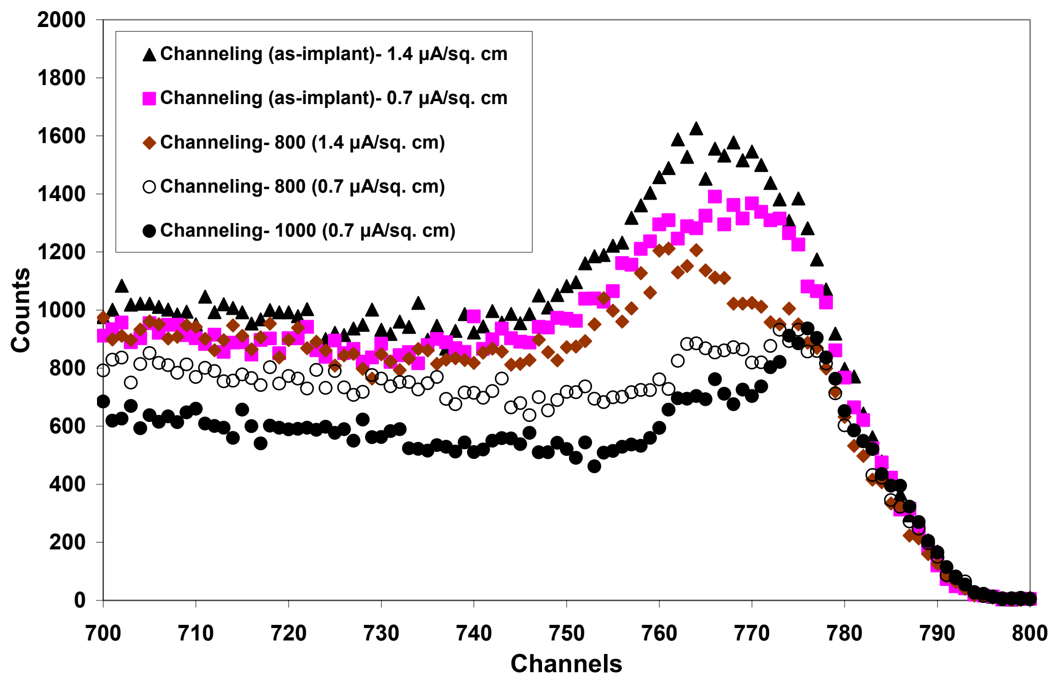

Figure 5.4. RBS and channeling spectra showing the trend of damage development in as-implanted and annealed samples with different ion current densities of 0.7 and 1.4 µA respectively, to a dose of 1Ч10^{15} In^+ ions/cm^2.

However, still there are very few studies same dealing directly with the re-crystallization of heavily damaged ZnO at high temperatures. Jeong *et al.* [37] presents an annealing study by As^+ implantation in single crystalline ZnO at room temperature involving the same dose (1×10^{15} ions/cm^2) as reported here. They annealed their samples at various temperatures and reported that annealing at 800 $^{\circ}$C for 60 minutes produced optimum recovery of crystalline quality [37]. Some dissimilarity can be observed between the two studies; with In^+ implantation in ZnO single crystal. It can be seen in Fig. 5.4 that after high temperature annealing up to 1000 $^{\circ}$C, some recovery occurred though a highly damaged layer with a reduced thickness remained. The RBS/C spectra in Fig. 5.4 also show that thermal annealing appears to effectively recover the crystalline quality of the implanted layer. In particular, the level of lattice disorder progressively decreased with increasing annealing temperature. The crystallinity of the ZnO with highest temperature could not be recovered completely as there remained a significant difference in channeling yield compared with the virgin spectrum in Fig. 5.1. After comparison of the spectrum of as-implanted and annealed samples at different ion current densities in Fig. 5.4, it was observed that the rate of defect production was higher in the case of higher ion current density 1.4 μA/cm^2 than for the lower one 0.7 μA/cm^2. This suggests that implantation ion current density enhances damage creation in bulk ZnO single crystal.

Figure 5.5 shows damage buildup tendency in In^+ implanted single crystal ZnO as a function of ion current density. The disorder raised the integrated intensity for as-implanted and annealed samples as a result of increasing ion current density. In this figure, highest damage intensity occurred after In^+ implantation for both cases, with different ion current densities. After thermal treatment, the damage intensity decreased in a systematic way with respect to ion current densities.

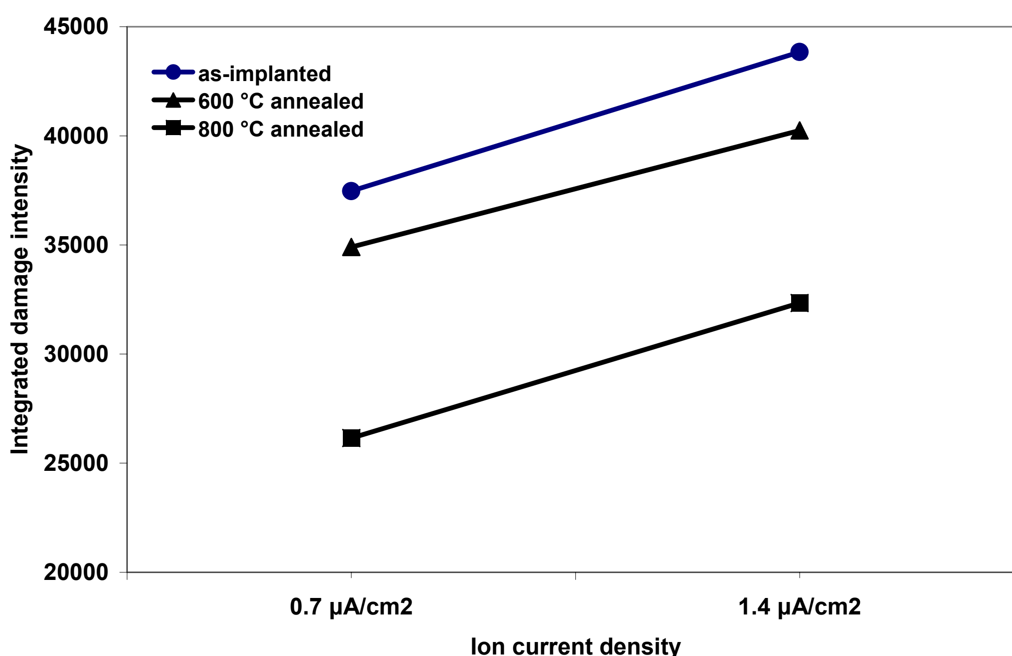

Figure 5.5. Comparison of damage intensity with respect to ion current density of as-implanted as well as after thermal treatment. The samples were bombarded at room temperature with 120 keV In^+ ions to a dose of $1Ч10^{15}$ cm^{-2}.

It is also clear from Fig. 5.5 that in the case of higher ion current density, the damage intensity for each sample was higher than for those in the case of lower ion current density, which suggests that damage creation inside the bulk ZnO single crystal is dependent on implantation ion current density.

Figure 5.6 shows the yields from Indium of as-implanted and annealed samples in random and channeling direction. It can be supposed from the random and channeling spectra of In peaks of as-implanted sample that many Indium atoms exist in the lattice site. The peak intensity of as-implanted Indium was calculated to have 1440 ± 40 counts in random case which was almost the same (1560 ± 40 counts) in channeling case after annealing the sample at 1000 $^{\circ}$C. It suggests that there were no Indium desorption at this temperature. In the case of as-implanted samples, the minimum yield of Indium was 30% which was little bit higher than that of substrate Zn. It also indicates that severe damage occurred in the bulk single crystal by In^{+} implantation.

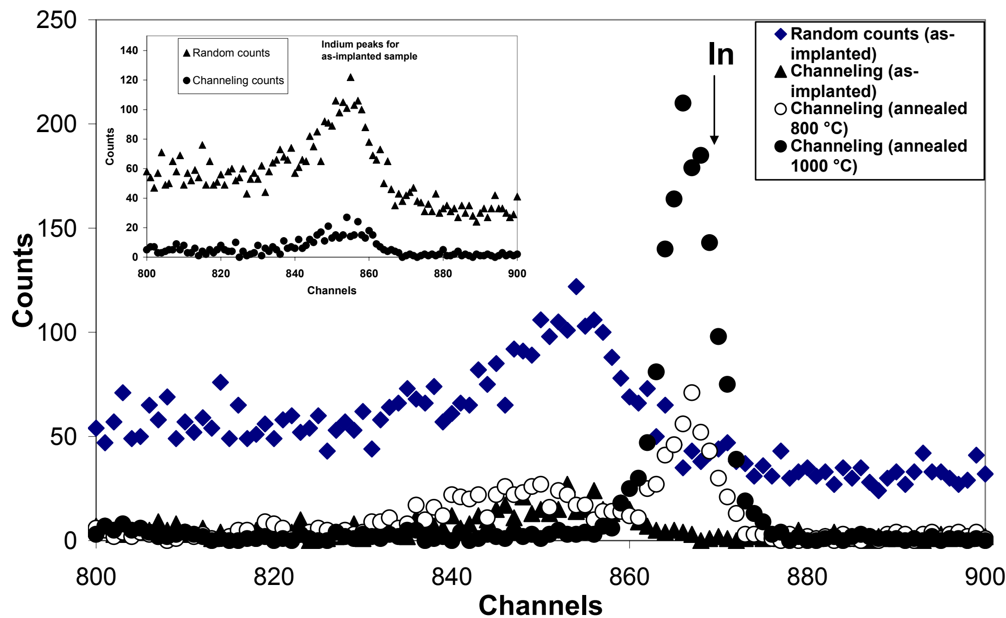

Figure 5.6. RBS/C spectra of Indium peaks for as-implanted and annealed samples. High background for random case is due to the so called pile-up effect.

After post-annealing at 600 $^{\circ}$C, Indium atoms did not change their position and located inside the bulk crystal. Location change began after annealing at 800 $^{\circ}$C as some of In atoms existed in the bulk as well as started to diffuse towards the surface and segregated there, but there were no In atoms in the bulk ZnO single crystal annealed at 1000 $^{\circ}$C.

5.5 Conclusion

We have studied the damage buildup behavior in ZnO single crystal bombarded with 120 keV In^{+} ions at a fluence of 1Ч10^{15} cm^{-2} with different implantation ion current densities 0.7 and 1.4 μA/cm^{2}, respectively. Our results

reveal that ion implantation produced defect in single crystal ZnO, as the minimum yield for as-implanted sample increased from 2.0 % to 18.0 % and 22.0 % which is an indication of degrading the crystalline quality. Thermal treatment after ion implantation led to improve the damage recovery. Damage recovery started after annealing the sample at 600 °C as the damage intensity reduced than as-implanted sample. It has been reported previously [37] that in As^{+} ion implantation with same dose (1×10^{15} cm^{-2}) that optimum recovery of crystallinity of ZnO occurred after annealing at 800 °C. In our study, after In^{+} implantation, optimum recovery could not be achieved after annealing at that temperature. It was observed that after post-annealing at high temperature 1000 °C, there remained some damage with reduced thickness in the bulk ZnO. Our results also show that implantation ion current density has a direct influence on damage buildup in single crystal ZnO. Higher ion current density raised the minimum yield from 18% to 22% which indicates that damage production in ZnO single crystal was increased by increasing implantation ion current density. The damage intensity of as-implanted and annealed samples also became higher as a result of increasing ion current density. The excitation life-time of In^{+} ions in our study was in the order of 10^{-5} sec. RBS/C spectra of Indium peaks of as-implanted samples indicate that In atoms are located in the lattice site. Some In atoms started to diffuse towards the surface after annealing at 800 °C. After post-annealing the sample at 1000 °C, there were no In atoms inside the bulk crystal; all had moved to the surface.

5.6 References

[1] S. O. Kucheyev, J. S. Williams and C. Jagadish, *Vacuum* **73**, 93 (2004).

[2] S. J. Pearton, D. P. Norton, K. Ip and Y. W. Heo, *J. Vac. Sci. Tech. B* **22**: 932, 2004.

[3] Y.W. Heo, M. P. Ivill, K. Ip, D. P. Norton, S. J. Pearton, J. G. Kelly, R. Rairigh, A. F. Hebard and T. Steiner, *Appl.Phys. Lett.* **84**, 2292 (2004).

[4] C. Coskun, D. C. Look, G. C. Farlow and J. R. Sizelove, *Semicond. Sci. Technol.* **19**, 752 (2004).

[5] S. O. Kucheyev, J. S. Williams, C. Jagadish, J. Zou, C. Evans, A. J. Nelson and A. V. Hamza, *Phys. Rev. B* **67**, 094 115 (2003).

[6] S. O. Kucheyev, J. S. Williams and C. Jagadish, *Vacuum* **73**, 93 (2004).

[7] S. J. Pearton, D. P. Norton, K. Ip, Y. Heo and T. Steiner, *J. Vac. Sci. Technol. B* **22**, 932 (2004).

[8] S. J. Pearton, D. P. Norton, K. Ip, Y. W. Heo and T. Steiner, *Prog. in Mater. Sci.* **50**, 293 (2005).

[9] F. D. Auret, S. A. Goodman, M. Hayes, M. J. Legodi, H. A. van Laarhoven and D. C. Look, *J. Phys. Cond. Mat.* **13**, 8989 (2001).

[10] [130] D. C. Look, D. C. Reynolds, J. W. Hempsky, R. L. Jones and J. R. Sizelove, *Appl. Phys. Lett.* **75**, 811 (1999).

[11] T. S. Jeong, M. S. Han, J. H. Kim, C. J. Youn, R. Y. Ryu and H. W. White, *J. Cryst. Growth* **275,** 541 (2005).

[12] E. Sonder, R. A. Zhur and R. E. Valiga, *J. Appl. Phys.* **63**, 1140 (1988).

[13] Z. Q. Chen, A. Kawasuso, Y. Xu, H. Naramoto, X. L. Yuan, T. Sekiguchi, R. Suzuki and T. Ohdiara, *J. Appl. Phys.* **97**, 013 528 (2005).

[14] K. Ip, M. E. Overberg, Y. W. Heo, D. P. Norton, S. J. Pearton, S. O. Kucheyev, C. Jagadish, J. S. Williams, R. G. Wilson and J. M. Zavada, *Appl. Phys. Lett.* **81**, 3996 (2002).

[15] T. S. Jeong, M. S. Han, C. J. Youn and Y. S. Park, *J. Appl. Phys.* **96**, 175 (2004).

[16] G. Xiong, K. B. Ucer, R. T. Williams, J. Lee, D. Bhattacharyya, J. Metson and P. Evans, *J. Appl. Phys.* **97**, 043 528 (2005).

[17] S. Limpijumnong, S. B. Zhang, S.-H. Wei and C. H. Park, *Phys. Rev. Lett.* **92**, 155 504 (2004).

[18] U. Wahl, E. Rita, J. G. Correia, A. C. Marques, E. Alves and J. C. Soares, *Phys. Rev. Lett.* **95,** 215 503 (2005).

[19] C. Boemara, T. Monteiro, M. J. Soares, J.G. Guilherme, and E. Alves, *Physica B* **308-310,** 985 (2001).

[20] K. Sato and H. Katayama-Yoshida, *Semicond. Sci. Technol.* **17,** 376 (2002).

[21] K. Sato and H. Katayama-Yoshida, *Jpn. J. Appl. Phys., Part 2* **40,** L334 (2001).

[22] K. Ueda, H. Tabata, and T. Kawai, *Appl. Phys. Lett.* **79,** 988 (2001).

[23] D.C. Look, J. W. hemsky, and J. R. Sizelove, *Phys. Rev. Lett.* **82,** 2552 (1999).

[24] F. Tuomisto, V. Ranki, K. Saarinen, and D. C. look, *Phys. Rev. Lett.* **91,** 205502 (2003).

[25] Yu. V. Gorelkinskii and G. D. Watkins, *Phys. Rev. B* **69,** 115212 (2004).

[26 C. Coskun, D. C. Look, G. C. Farlow, and J. R. Sizelove, *Semicond. Sci. Technol.* **19,** 752 (2004).

[27] F. D. Auret, S. A. Goodman, M. Hays, M. J. Legodi, H. A. Van Larrhoven, and D. C. Look, *Appl. Phys. Lett.* **79,** 3074 (2001).

[28] A. Y. Polyakov, N. B. Smirnov, A. V. Govorkov, E. A. Kozhukhova, V. I. Vdovin, K. Ip, M. E. overberg, Y. W. Heo, D. P. Norton, S. J. Pearton, J. M. Javada, and V. A. dravin, *J. Appl. Phys.* **94,** 2895 (2003).

[29] S. O. Kucheyev, J. S. Williams, C. Jagadish, J. Zou, C. Evans, A. J. Nelson, and A. V. Hamza, *Phys. Rev. B* **67,** 094115 (2003).

[30] E. Alves, E. Rita, U. Wahl, J. G. Correia, T. Monteiro, J. Soares, and C. Boemare, *Nucl. Instrum. Methods Phys. Res. B* **206,** 1047 (2003).

[31] T. S. Jeong, M. S. Han, C. J. Youn, and Y. S. Park, J. Appl. Phys. **96,** 175 (2004).

[32] F. Reus, C. Kirchner, Th. Gruber, R. Kling, S. Maschek, W. Limmer, A. Wagg, and P. Ziemann, *J. Appl. Phys.* **95,** 3385 (2004).

[33] S. J. Pearton, D. P. Norton, K. Ip, Y. W. Heo, and T. Steiner, *J. Vac. Sci. Technol.* B **22,** 932 (2004).

[34] K. Lorenz, E. Alves, E. Wendler, O. Bilani, W. Wesch, and M. Hayes, *Appl. Phys. Lett.* **87,** 191904 (2005).

[35] T. Monteiro, C. Boemare, M. J. Soares, E. Rita, and E. Alves, *J. Appl. Phys.* **93,** 11 (2003).

[36] G. Battistig, J. G. Lopez, Y. morilla, N. Q. Khanh, T. Lohner, P. Petrik and A. R. Ramos, *Nucl. Instrum. Methods Phys.Res.B,* **219,** 652 (2004).

[37] T. S. Jeong, M. S. Han, J. H. Kim, C. J. Youn, R. Y. Ryu and H. W. White, *J. Cryst. Growth,* **275,** 541 (2005).

CHAPTER 6

Effect of ion dose on defects formation in ZnO

6.1. Introduction

ZnO is an interesting II-VI semiconductor material with an exciton binding energy of 60 meV and which has a wide-band-gap energy (E_g ~ 3.37 eV at room temperature) being transparent in the visible light region [1]. It has therefore been considered a promising candidate for the development of light emitting structures and lasers of the blue and ultraviolet. Besides these unique optical and electrical properties, it was reported that defect generation rate is lower than other transparent semiconductors such as GaN [2,3].One of most promising fabrication methods in materials research is ion implantation because it is a non-thermodynamic approach and so allows production of a high metal filling factor in a solid matrix, beyond the equilibrium limit of solubility [4]. This technique has high controllability and reproducibility but the implanted materials show complex phenomena that are dependent on environment and temperature ramp rates as well as temperature and time [5].

Ion implantation causes crystallographic damage as each individual ion produces many point defects in the target crystal on impact such as vacancies and interstitials. Damage formation by ion implantation depends on various parameters such as substrate temperature, ion beam energy, ion current density etc. However, successful optical activation and lattice recovery have been achieved by ion implantation in GaN [6]. Deep-level structure-less emissions

are commonly observed in undoped ZnO single crystals [7, 8], powder samples [9, 10], thin films [11, 12] and nano-crystalline particles [13]. The centers for the unstructured emission bands in the green, yellow and red spectral regions are usually assumed to be due to different native defects in ZnO such as oxygen vacancy (V_o), zinc vacancy (V_{Zn}), interstitial zinc, interstitial oxygen and antisite defect (O_{Zn}) [7- 13]. Still there is no consensus in the literature concerning the nature of the defects where luminescence originates. In this paper, optical properties and damage profile has been studied for a high quality ZnO single crystals with In^+ implantation.

6.2. Experimental methods

Single crystal bulk wurtzite ZnO samples used in this study were purchased from MTI Co., USA. As specified by the grower, the samples were nominally undoped, (0001) oriented, single side (Zn-face) polished. The dimension of each crystal was 10 mm Ч 10 mm Ч 0.5 mm. In^+ ions were implanted under an acceleration voltage of 120 keV, at room temperature with ion current density of 0.7 μA cm^{-2}. During implantation, samples were tilted by 7° relative to the incident ion beam to prevent channeling.

Three different dosages: 1Ч10^{14}, 3Ч10^{14} and 1Ч10^{15} ions.cm^{-2}, respectively were chosen in commercial aspects. A post-implantation annealing was carried

out to electrically activate the dopant species and crystal defects due to ion bombardment. To study the optical properties after implantation, the ZnO single crystal was divided into four smaller samples, one of them was an as-implanted sample and the other three samples were annealed at 600 $^{\circ}$C, 800 $^{\circ}$C and 1000 $^{\circ}$C in air for 60 minutes, respectively. Rutherford Backscattering Spectrometry and Channeling techniques (RBS/C) were performed to investigate the crystalline quality and dose dependence on damage formation inside the bulk ZnO single crystal.

RBS/C measurements were performed using the 4 MeV Van de Graaff-type accelerator located at Hiroshima University, Japan. For these experiments, a collimated 2 MeV $^{4}He^{+}$ ion beams were used and a silicon surface barrier detector with a resolution of 15 keV was set at an angle of 165° to collect the backscattering helium ions as shown in Fig. 6.1. The diameter of the $^{4}He^{+}$ ion beams was typically 2 mm. The beam current was around 10 nA. The total dose of He^{+} was fixed at 20 μC. The signal was recorded through a low capacitance charge amplifier. Moreover, in order to prevent channeling conditions, the samples were tilted by 5° with the normal during RBS measurements. The samples were aligned to the crystal axis <0001> to investigate the crystal damage formation. The pressure inside the vacuum chamber during the experiments was about 10^{-7} mbar.

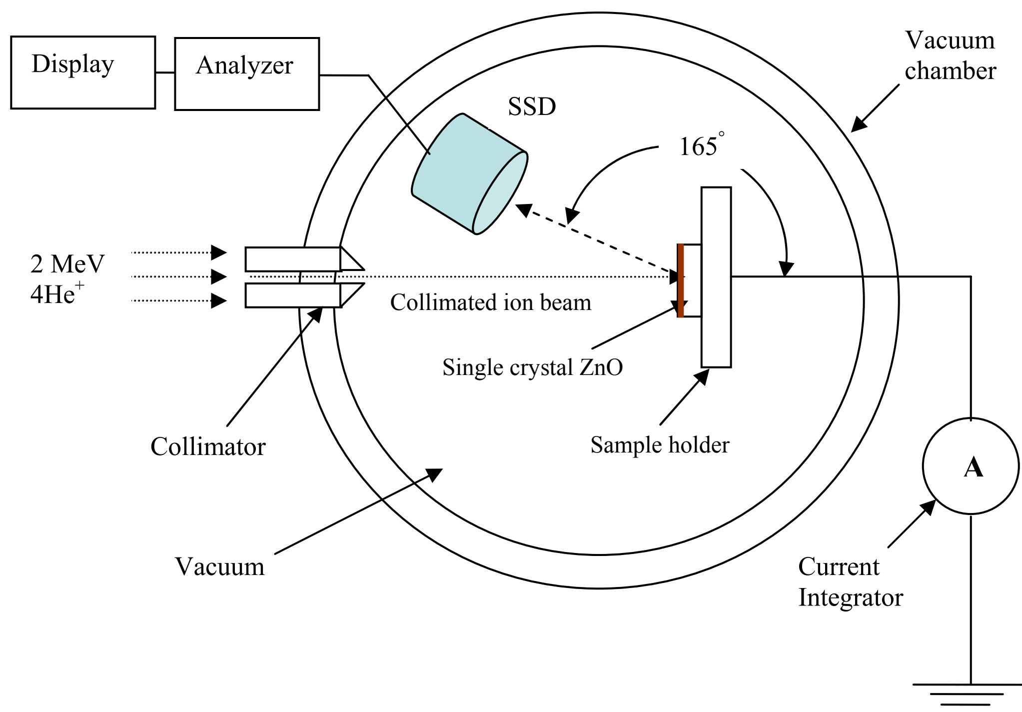

Figure 6.1. Experimental setup for RBS/C measurements to investigate the damage formation with different doses in ZnO single crystals.

The virgin, as-implanted and annealed samples were characterized from photoluminescence (PL) spectra to estimate the recovery from radiation damage in the ZnO lattice. This investigation is motivated by the need to further understand the effects of damage resulting from the implantation process on the PL of ZnO. Photoluminescence measurements were carried

out at room temperature with a 325-nm cw He-Cd laser with an excitation power of 20 mW. Every sample got an exposure around 8 mW and the luminescence detection system was conducted with a Horiba Jobin Yvon spectrometer, coupled to a CCD camera. The PL setup is shown in Fig. 6.2.

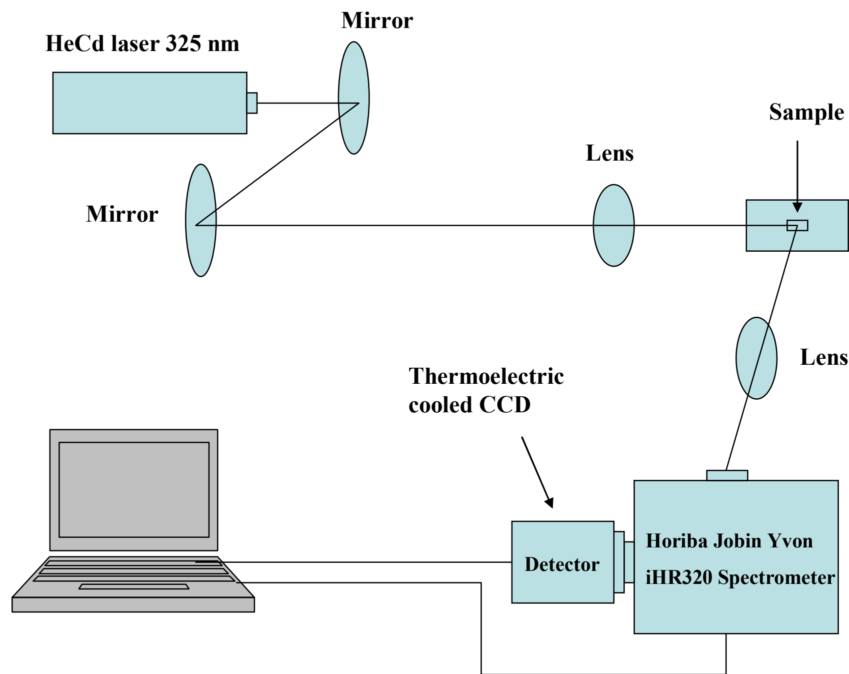

Figure 6.2. Schematics of Photoluminescence measurements to investigate the damage recovery of In^{+} implanted single crystal ZnO.

6.3. Results and discussion

The main feature of this study is to investigate the damage buildup behavior as a function of ion dose. Figure 6.3 shows the random and <0001> aligned RBS spectra for the virgin single crystal ZnO. The surface edge of substrate oxygen and Zn can be observed here. The reduced Zn signal in the channeling spectrum, when compared with random acquisition yield, indicates the excellent crystalline quality of the bulk ZnO.

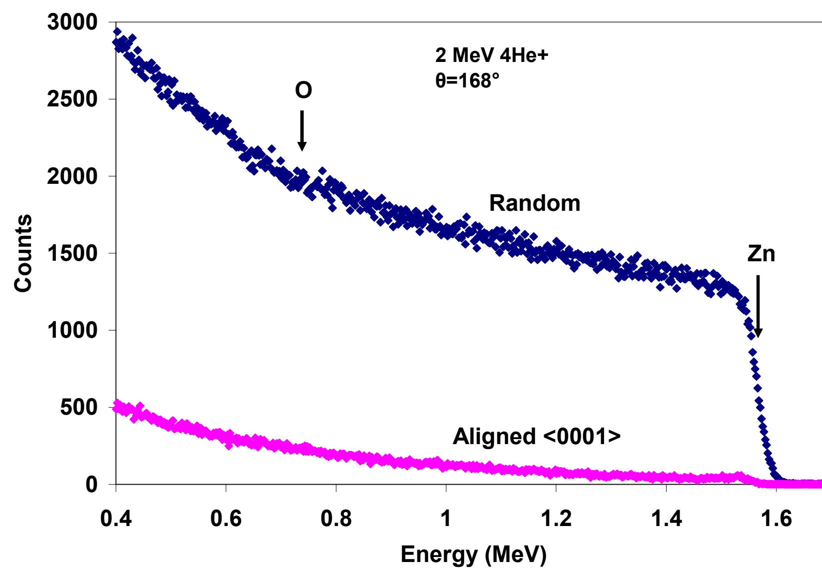

Figure 6.3. Comparison of RBS and channeling spectra of un-implanted bulk single crystal ZnO.

For this un-implanted single crystalline ZnO, the minimum yield (χ_{min}) is only 2.0 % which indicates good crystallinity.

Figure 6.4 shows the RBS and <0001> aligned spectra of In^+ implanted single crystal ZnO with fluence of 1Ч10^{14} ions/cm^2. As a measure of damage concentration, the minimum yield χ_{min} was calculated within a window (channels 750-770) which can evaluate the crystalline quality with different treatments such as by ion implantation, deposition and annealing. To calculate the damage level created by In^+ ion implantation, the yields of the aligned spectrum comprising the whole implanted layer were integrated as indicated in Fig. 6.4. In this figure, the minimum yield, χ_{min} was calculated from that window to be as large as 7% which indicates that damage was produced in the implanted layer, so that, the crystalline quality of bulk ZnO became degraded by In^+ implantation as compared with that of the virgin crystal in Fig. 6.3. The integrated intensity of damage shoulder was calculated to consist of 16,500 counts. It is interesting that for a dose of 1Ч10^{14} ions/cm^2 by In^+ implantation, the smallest dose used in the present study, RBS/C is essentially distinguishable from spectra for virgin sample but Kucheyev *et al.* [14] reports by Au implanted ZnO single crystal that both RBS/C spectra from un-implanted sample and implanted sample at a fluence of 8Ч10^{13} cm^{-2} were the same which means no damage was developed by that dose. From their study, they also mentioned that the RBS/C spectra indeed had an additional peak between the expected surface and bulk defect peaks which is inconsistent with our result as there was no existence of such kind of additional peak by In^+ implantation.

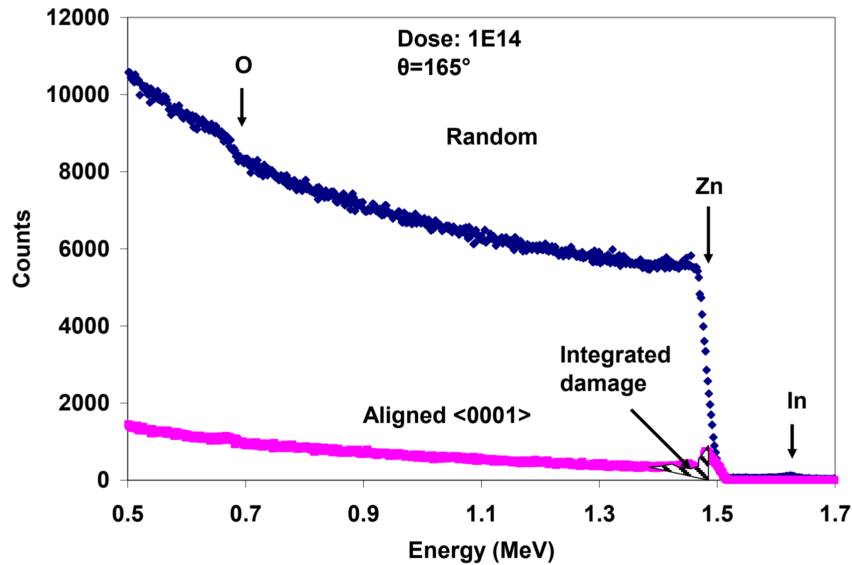

Figure 6.4. The RBS/C spectra of ZnO single crystal after In^+ implantation at a fluence of 1Ч10^{14} ions/cm^2 with ion current density 0.7 μA/cm^2. The implantation was done at room temperature, under an accelerating voltage of 120 keV.

Random and [0001]-aligned RBS spectra of In^+ implanted single crystals ZnO with different dosage are shown in Figure 6.5. In this experiment, the sample had received an In^+ implant fluence of 3Ч10^{14} ions/cm^2. With this ion dose, the damage raised the minimum yield χ_{min} of bulk crystal, from 2% to 11% which is greater than that for lower ion dose (1Ч10^{14} ions/cm^2). It suggests that crystalline quality also became worse than in the previous case (Fig. 6.4) as well as damage buildup in ZnO single crystal was increased to some extent.

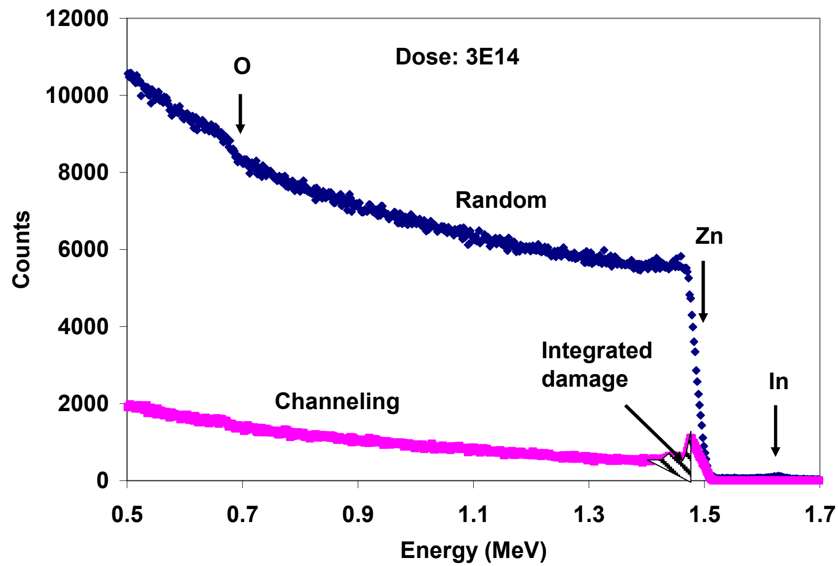

Figure 6.5. RBS and <0001> aligned spectra of single crystal ZnO after room temperature In^+ implantation with an ion beam energy of 120 keV and ion current density 0.7 μA.cm^{-2}. In this case, implantation dose was 3Ч10^{14} ions/cm^2.

The integrated damage intensity with an ion dose of 3Ч10^{14} cm^{-2} , was higher (25,540 counts) than that which occurred with less than this dose. This indicates that the level of bulk disorder gradually increases as a result of increasing ion dose size.

Figure 6.6 shows the RBS and aligned spectra of In^+ implanted single crystal to the highest fluence of 1Ч10^{15} ions/cm^2 at room temperature with ion beam energy of 120 keV and beam current density 0.7 μA.cm^{-2}. In this case, the normalized yield of the substrate raised 18% and integrated damage intensity

(45,820 counts) also higher than that developed for those doses less than this relatively larger dose which resulted from increasing the amount of relative disorder. Similar studies have been carried out by other groups of researchers for the case of Au [14] and Cu [15, 16] implanted ZnO single crystals, respectively. Kono *et al.* [15] presents a study of Cu implants into ZnO single crystal under low beam energy (60 keV) with ion current density of 2.0 $\mu A.cm^{-2}$. From their RBS/C results, it was claimed that the χ_{min} of as-irradiated sample remains 10% to a dose of 1×10^{15} ions/cm^2, which is lower than that calculated from our study with the same dose by In^+ implantation. Therefore, it can be concluded that heavy elements can create relatively larger damage in bulk single crystal ZnO.

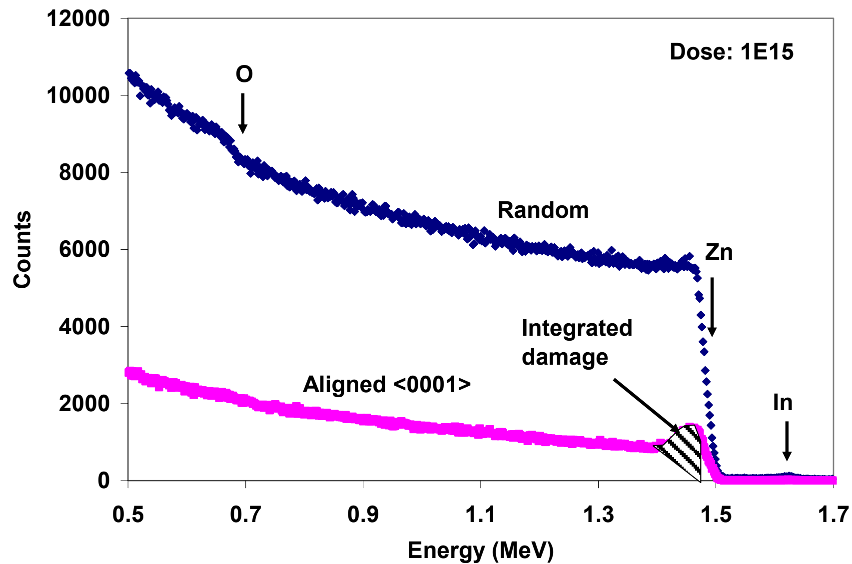

Figure 6.6. RBS and <0001> aligned spectra of single crystal ZnO after In^+ implantation under an acceleration voltage of 120 keV and ion current density 0.7 $\mu A.cm^{-2}$. In this case, implantation was done at room temperature at a fluence of 1Ч10^{15} ions/cm^2.

Figure 6.7 shows RBS/C spectra illustrating the damage buildup in ZnO single crystal bombarded at room temperature with 120 keV In^+ ions. It can be seen in Fig. 6.7 that ion-beam-produced lattice defects are apparently bimodal. Indeed, this figure shows that lattice disorder in the Zn sub-lattice accumulates both in the crystal bulk and near the sample surface. Such bimodal damage profiles are not uncommon for ion implanted semiconductors, for which disorder typically accumulates in the crystal bulk (where the nuclear energy-loss profile is maximum) and at the sample surface (which is often a sink for ion beam generated point defects) [17, 18].

Figure 6.7 also reveals a shift of the position of the bulk defect peak to lower backscattering energies with increasing ion dose which enhances the level of lattice disorder. Such a shift can partly be attributed to the difference in the energy loss of the analyzed He ions for random and aligned directions. It can be observed clearly in Fig. 6.7 that bulk disorder gradually increases with increasing ion dose. However, such an increase in the level of ion beam produced lattice damage for relatively large ion dose can be attributed to ion-beam-induced material decomposition [14]. They also reported that a wide surface peak was observed for ion dose $< 5\times10^{14}$ ions/cm^2 and that an additional peak existed between the surface and bulk defect peaks for ion doses $< 1\times10^{16}$ ions/cm^2; this is inconsistent with our study in this dose range. A broad surface peak is observed for ion dose 1×10^{15} ions/cm^2, and other RBS/C spectra for less than this dose have no additional peak, as shown in Fig. 6.7. Interestingly, Fig. 6.7 shows that as ion dose increases, the defect peak originates at the sample surface and moves toward the bulk crystal. From a study of XTEM image [14] it has been reported that the microstructure of ion-beam-produced defects consisting of some point defect clusters and some planar defects exist parallel to the basal plane of the ZnO wurtzite structure. They also mentioned that for a dose of 1×10^{15} ions/cm^2, a band of planar defects is observed in a near surface layer. This is also the largest dose used in our study for which the integrated damage intensity was the highest as compared with other samples and it may be happened due to the above reasons.

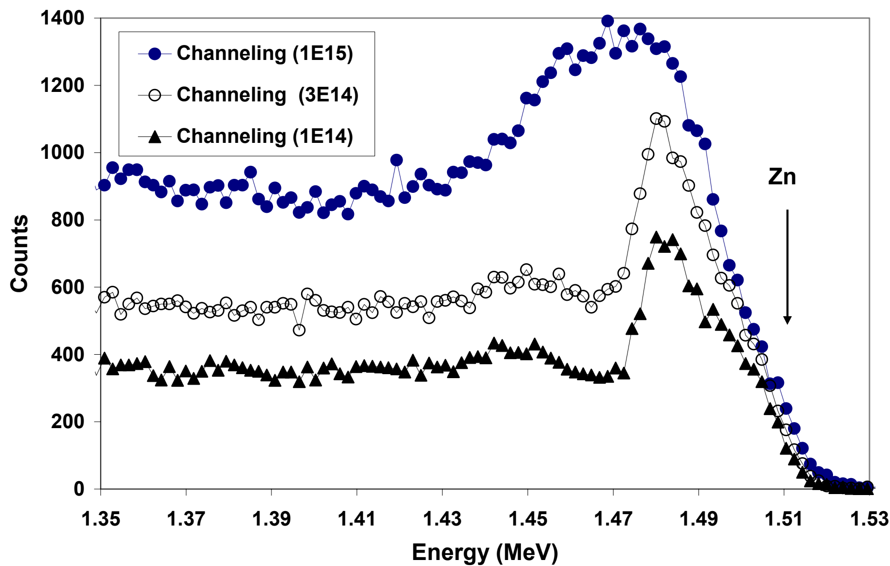

Figure 6.7. RBS and channeling spectra show the trend of damage buildup in single crystal ZnO by In^+ implantation. The ion dose was varied as 1Ч10^{14}, 3Ч10^{14} and 1Ч10^{15}/cm^2 respectively, at room temperature.

However, if the dose is comparatively lower, a dynamic annealing can take place. A steady state concentration of defects is reached when the recombination of interstitial and vacancy becomes equal to the generation rate. As the total dose increases, additionally created defects cause collapse of the damaged zone and create a large disordered zone, effectively enhancing the damage buildup in the bulk crystal.

The variation of minimum yields of as-implanted and annealed samples as a function of annealing temperatures is illustrated in Fig. 6.8. It is seen from this figure that the minimum yield gradually decreases with increasing annealing

temperature. Before annealing, the χ_{min} for as-implanted ZnO single crystal was 22% indicating the degradation of crystallinity. After post-annealing at 600 °C, χ_{min} became 18% which suggests that re-crystallization started to occur at this temperature. Then it reduced to be 12% after post-implantation annealing of the implanted sample at 800 °C which means that crystalline quality became improved than previous case. Finally, it dropped to 7% after thermal treatment at 1000 °C. It suggests that thermal treatment recovered the damage created in the implanted layer by In^+ implantation and enhancing the improvement of crystalline quality of bulk ZnO.

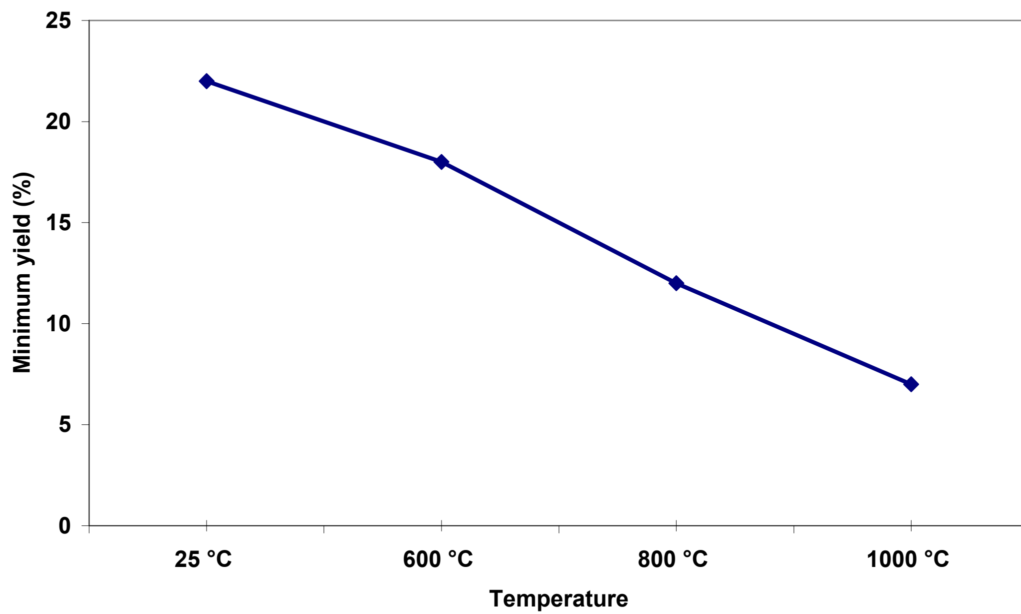

Figure 6.8. Plot of minimum yield, χ_{min} of In implanted single crystal ZnO as a function of annealing temperature. Implantation has been done at room temperature with 120 keV to a dose of 1Ч10^{15} ions/cm^2 while ion current density was 1.4 μA/cm^2.

The RBS and channeling spectra of the damage recovery of ZnO after In^+ implantation are illustrated in Figure 6.9. The trend of disorder is clearly visible in this picture. The thickness of the damaged layer reduced due to annealing indicating that some re-crystallization may occur near to the implanted/non-implanted interface. Jeong et al. (4) reported for As^+ implanted ZnO single crystal in the same condition as ours where they mentioned that an annealing at 800 °C for 60 minutes produced optimum recovery of crystallinity.

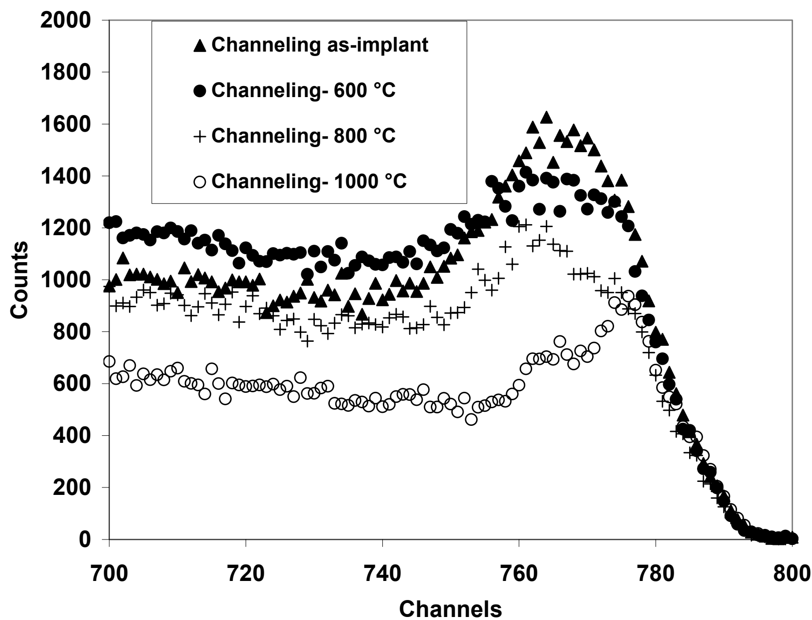

Figure 6.9. RBS/C spectra show the damage buildup and its recovery as a function of annealing temperature in an In implanted single crystal ZnO. Implantation has been done at room temperature at a fluence of 1Ч10^{15} ions/cm^2 under acceleration voltage of 120 keV whilst ion current density was 0.7 μA/cm^2.

Some dissimilarity can be observed from this study with In^+ implantation. It can be seen from Fig. 6.9 that after high temperature annealing up to 1000 $^{\circ}$C, maximum recovery occurs though a damaged layer with reduced thickness remains. The RBS/C spectra also show that heat treatment appears to effectively recover the crystalline quality of the implanted layer. In particular, the level of lattice disorder progressively decreases by means of increasing annealing temperature. The re-crystallization of ZnO with the highest temperature could not be recovered perfectly as there remains a significant difference in channeling yield compared with the virgin spectrum in Fig. 6.3.

The room temperature PL spectra were obtained from a series of In^+ implanted and non-implanted ZnO samples recorded in a wavelength range from 300 to 800 nm but only the interesting region is shown here in Figure 6.10. All samples show a band edge emission at 375 nm and other contributions in the visible region. It is clearly visible that the PL emission was completely extinguished by room temperature implantation. This means that the radiation damage acted as a non-radiative defect. Heat treatment leads to a recovery of PL intensity. It can be seen from Fig. 6.10 that after the annealing of the sample at 1000 $^{\circ}$C, the PL intensity was increased to closer to the maximum bulk intensity which suggests that at this temperature bulk disorder reduced to be the minimum. For the as-implanted sample, the PL intensity was the minimum but it increased gradually with increasing temperature, which is

clearly observed from these PL spectra due to those samples being annealed at 600 and 800 °C, respectively. Another interesting feature of these results is that the maximum emission originated in the same wavelength at 375 nm both for un-implanted and 800 °C annealed sample, which indicates that the preferred annealing temperature for single crystal ZnO is 800 °C. These results indicate that the recovery from radiation damage by annealing led to the formation of deep level defects.

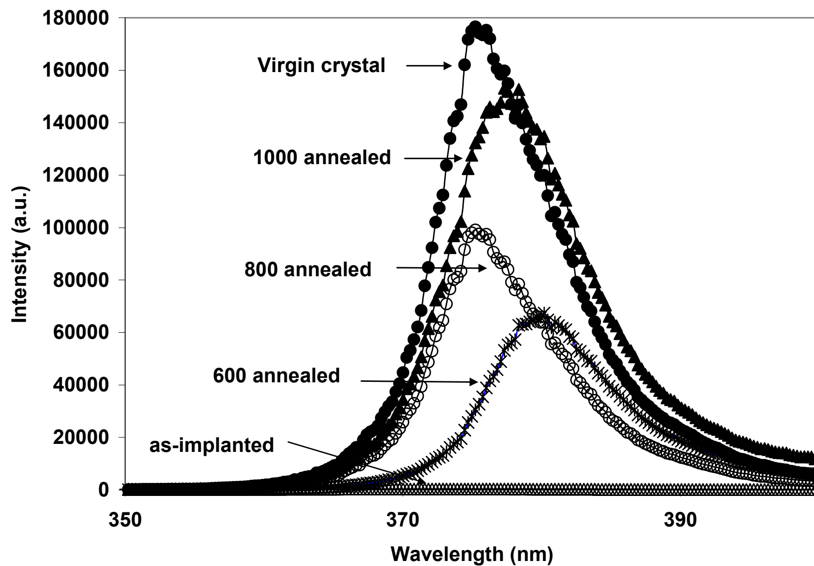

Figure 6.10. Room temperature PL spectra of virgin, as-implanted and annealed ZnO samples. The samples were bombarded at room temperature with 120 keV In^+ ions to a dose of 1Ч10^{15} cm^{-2} and annealed at 600, 800 and 1000 °C in air for 60 minutes.

Our photoluminescence results are consistent with our previous RBS/C study for damage recovery of single crystal ZnO. However, the shift of PL peaks with temperature, an unusual trend, is also observed in Fig. 6 (b). Additional low-temperature photoluminescence studies may be carried out to clarify this kind of shift. It has been claimed by Vanheusden *et al.* [9] that oxygen vacancies are responsible for the blue/green luminescence in ZnO. Oxygen vacancies may occur in three different charge states such as V_o, $V^{/}_o$ and $V^{//}_{o,}$ but only the singly ionized oxygen vacancy ($V^{/}_o$) can act as the luminescence center in single crystal ZnO. The above suggests the possibility to generate this kind of emission due to oxygen vacancies introduced by In^+ implantation and also our samples were annealed in an oxidizing atmosphere.

6.4 Conclusion

We have studied damage buildup behavior in ZnO single crystal bombarded with 120 keV In^+ ions to a dose range of 1×10^{14} to 1×10^{15} cm^{-2} with implantation ion current densities 0.7 $\mu A/cm^2$. Our results reveal that damage buildup in bulk ZnO single crystal depends on the dose size. The minimum yield for as-implanted sample increased from 7.0 % to 18.0 % which is an indication of degradation of crystalline quality. The damage intensity of implanted samples gradually increased as a result of increased ion dosages. Kono *et al.* [15] claimed that 1×10^{16} $ions/cm^2$ is the tolerance dose limit up to

which, no significant damage occurred in bulk single crystal ZnO, but in our study for an ion dose of 1Ч10^{15}/cm^{2}, significant bulk disorder produced as the χ_{min} raised 18% which is larger than that obtained (10%) for the same dose from their study. Heat treatment after ion implantation led to improve the damage recovery as the PL intensity gradually increased with increasing temperature. Jeong *et al.* [19] reported with As^{+} ion implantation using same dose (1Ч10^{15} cm^{-2}) that optimum recovery of crystallinity of ZnO occurred after annealing at 800 $^{\circ}$C. From our PL study, after In^{+} implantation, maximum damage recovery could not be achieved after annealing at this temperature. It was observed from the PL spectra, after post-annealing at high temperature 1000 $^{\circ}$C, the intensity was maximum which indicates that the damage was minimum. Our PL study was consistent with our previous RBS/C study for damage recovery. However, it is noted that 800 $^{\circ}$C may be the perfect annealing temperature for single crystal ZnO as the maximum band edge emission occurred in the same wavelength at 375 nm for both virgin and 800 $^{\circ}$C annealed samples.

6.5 References

1) C. Boemara, T. Monteiro, M. J. Soares, J.G. Guilherme, and E. Alves, *Physica B* **308-310,** 985 (2001).

2) D.C. Look, D.C. Leynold, J. W. Hemsky, R. L. Jones, J. R. Sizelove, *Appl. Phys. Lett.* **79,** 3074 (2001).

3) D.C. Look, *Mater. Sci. and Eng. B.* **80,** 383 (2001).

4) P. D. Townsend, P. J. Chandler, L. Zhang, *Optical Effects of Ion Implantation,* Cambridge University Press, Cambridge, 1994 and 2006.

5) C. W. Whitw, L.A. Boatner, P. S. Skald, C. J. McHargue, J. Rankin, G. C. Farlow, M. J. Aziz, *Nucl. Instr. And Meth. B.* **32,** 11 (1988).

6) E. Alves, K. K. Lorentz, R. R. Vianden, C. Boemare, M. J. Soares, T. Monteiro, *Mod. Phys. Lett. B.* **28-29,** 1281 (2002).

7] S. Takata, T. Minami, H. Nanto, T. Kawamura, *Phys. Status. Solidi A.* **65,** K83 (1981).

8) F. Leiter, H. Zhou, F. henceker, A. Hofstaetter, D. M. Hoffmann, B. K. Meyer, *Physica B.* **308-310,** 908 (2001).

9) K. Vanheusden, W. L. Warren, C. H. Seager, D. R. Tallant, J. A. Voigt, B. E. Gnade, *J. Appl. Phys.* **79,** 7983 (1996).

10) C. Gaspar, F. Costa, T. Monteiro, *J. Mater. Sci.: Mater. Electron.* **12,** 269 (2001).

11) B. Lin, Z. Fu, Y, Jia, G. Liao, *J. Electrochem. Soc.* **148,** G110 (2001).

12) S. A. Studenikin, N. Golego, M. Cocivera, *J. Appl. Phys.* **84,** 2287 (1998).

13) A. van Dijken, E. A. Meulenkamp, D. Vanmaekelbergh, A. Meijerink: *J. Lumin.* **90,** 123 (2000).

14) S. O. Kucheyev, J. S. Williums, C. Jagadish, J. Zou, C. Evans, A. J. Nelson, A.V. Hamza: *Phys. Rev. B.* **67,** 094115 (2003).

15) K. Kono, S. K. Arora, N. Kishimoto: *Nucl. Instr. And Meth. B.* **206,** 291-294 (2003).

16) A. Cetin, R. Kibar, M. Ayvacikli, N. Can, Ch. Buchal, P. D. Townsend, A. L. Stepanov, T. Karali, S. Selvi: *Nucl. Instr. And Meth. B.* **249,** 474-477 (2006).

17) S. O. Kucheyev, J. S. Williums, C. Jagadish, J. Zou, G. Li, A. I. Titov: *Phys. Rev. B* **64,** 035202 (2001).

18) S. O. Kucheyev, J. S. Williums, C. Jagadish, J. Zou, G. Li: *Phys. Rev. B.* **62,** 7510 (2000).

19) T. S. Jeong, M. S. Han, J. H. Kim, C. J. Youn, R. Y. Ryu, H. W. White: *J. Cryst. Growth.* **275,** 541 (2005).

CHAPTER 7

Ion beam produced damage under different acceleration energies and Hall-effect measurements

7.1 Introduction

Ion implantation is a high technology approach for modifying surface properties of materials. It is similar to a coating process, but it does not involve the addition of a layer on the surface. Originally developed for use in semiconductor applications, and still used extensively in that capacity today, ion implantation uses highly energetic beams of ions to modify surface structure and chemistry of materials at low temperature. The process does not adversely affect component dimensions or bulk material properties. Many surface properties can be improved with ion implantation including hardness and wear resistance, resistance to chemical attack, and reduced friction. The process can be applied to virtually any material, including most metals, ceramics and polymers; however, the effects of the process are typically material-specific.

Ion implantation offers numerous advantages for treating component surfaces. A primary benefit is the ability to selectively modify the surface without detrimentally affecting bulk properties, largely because the process is carried out at low substrate temperatures. The process is also extremely controllable and reproducible and can be tailored to modify different surfaces in desired ways.

The interactions of the energetic ions with the material modify the surface, providing it with significantly different properties than the remainder of the material. Specific property changes depend on the selected ion beam treatment parameters, for instance the particular ion species, energy, and total number of ions that impact the surface. It has been reported recently with our previous work [1] that ion current density has also direct influence on damage formation in ZnO. In this chapter, the damage accumulation tendency in ZnO single crystal under different acceleration energies will be discussed.

The room temperature Hall mobility in ZnO single crystals is on the order of 200 cm^2 v^{-1} s^{-1} [2]. ZnO normally has a hexagonal (wurtzite) crystal structure with a = 3.25 E and c = 5.12 E. Electron doping by ion implantation produces defects in ZnO and these defects originates from Zn interstitial in the ZnO lattice [3]. The intrinsic defect levels that lead to n-type doping lie approximately 0.05 eV below the conduction band. High electron carrier density can also be realized via group III substitutional doping. While n-type ZnO is easily realized via excess Zn or with Al, Ga or In doping, p-type doping has proven difficult to achieve. Minegishi et. al. has reported that it is possible the growth of p-type ZnO by the simultaneous addition of NH_3 in hydrogen carrier gas with excess Zn [4]. However, the resistivity of these films was high with $\rho \sim 100$ Ωcm which suggest that the mobile hole concentration was very low. Another work by Rouleau et. al. [5] on N doping into ZnO films shows

that N incorporation does not necessarily yield p-type behaviour. In this case, nitrogen doping in epitaxial ZnO films was achieved using a RF nitrogen plasma source in conjunction with pulsed laser deposition. However, they showed no p-type behaviuor as determined by Hall measurements. The Madelung energy decreases with n-type doping which is consistent with experimental results for electron doping with Al, Ga or In [6]. With N doping for holes, the Madelung energy increases, with significant localization of the N states. The theory does predict that co-doping N with Ga to form an N-Ga-N complex can decrease the Madelung energy and delocalize the N states, thus facilitating hole doping. Using pulsed laser deposition, Josef et. al. has reported that p-type behaviour in ZnO thin films prepared by co-doping Ga and N [7]. Electrically active N was achieved by passing N_2O gas through an electron cyclotron resonance plasma source. The authors claimed low resistivity ($\rho = 2\ \Omega$cm, carrier density ~ 4Ч $10^{19}/cm^3$) p-type ZnO co-doped with Ga and N in which Ga concentration ranged from 0.1% to 5%. Unfortunately, these results have proven highly sensitive to processing conditions and have been difficult to reproduce. While there have been significant efforts focusing on nitrogen doping, just one or two works reported for either As or P doping. However, p-n junction-like behaviour was reported for n-type ZnO in which the surface was heavily doped with phosphorus [8]. Laser annealing of a zinc phosphide-coated ZnO single crystal surface achieved the doping. A related result was reported for epitaxial ZnO films on

GaAs subjected to annealing [9]. In this case, a p-type layer was produced at the GaAs/ZnO surface. Both of these reports are promising, but present several unresolved issues related to the solid solubility of the dopant (ionic radii of As and P much larger than that for O) and possible secondary phase formation in the doped region.

ZnO is also promising for spintronic applications. Diet et. al. [10] predicted a Curie temperature of ≥ 300 K for Mn doped ZnO, while electron doping of Fe, Co or Ni doped ZnO was predicted to stabilize high Curie temperature ferromagnetism [11, 12]. Carrier induced ferromagnetism was predicted for the case of hole doping of ZnO(Mn) [13, 14], while methods for improving p-type doping have also been suggested [15]. Numerous reports of the magnetic properties of transition metal-doped ZnO have appeared recently [16- 20]. But almost no reports available so far with direct dealing with electrical properties of In implanted ZnO. From this point of view, another attempt was taken to investigate the electrical properties of Indium implanted single crystal ZnO, which will also be presented in this chapter.

7.2 Experimental methods

Single crystal bulk wurtzite ZnO samples used in this study were purchased from MTI Co., USA. As specified by the grower, the samples were nominally undoped, (0001) oriented, single side (Zn-face) polished. The dimension of

each crystal was 10 mm Ч 10 mm Ч 0.5 mm. To study the defects formation tendency under different acceleration energy, In ions were implanted at room temperature to a fluence of 3Ч10^{14}/cm^2, with an ion current density of 0.7 μA cm^{-2} while the accelerating voltages were varied 60, 120, 200 and 300 keV, respectively. Then to study the electrical properties of ion implanted ZnO, In ions were implanted to a dose of 1Ч10^{15}/cm^2 with the same ion current density under an acceleration voltage of 120 keV. In this case also, implantation was done at room temperature. During implantation, samples were tilted by 7° relative to the incident ion beam to prevent channeling.

The damage buildup behaviour has been investigated by means of Rutherford Backscattering Spectroscopy and Ion Channeling (RBS/C) techniques. RBS/C experiments have been performed at Hiroshima University using 2.5 MV Van de Graaff accelerator with normal laboratory arrangement. The electrical properties have been investigated by four-point-probe method. The Hall measurements were conducted by means of Accent HL5500 Hall System installed in Professor Tetsuya YAMAMOTO's lab of KUT Research Institute.

7.3 Results and discussion

Figure 7.1 shows the simulations of $^4He^+$ ion beam incident on a 0.5 mm thick In implanted single crystal ZnO which illustrate the elastic interactions of the

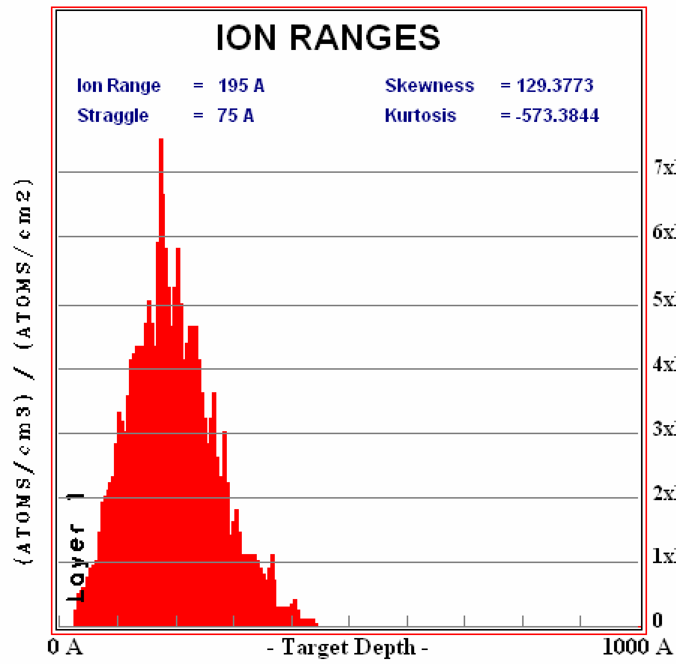

7.1 (a)

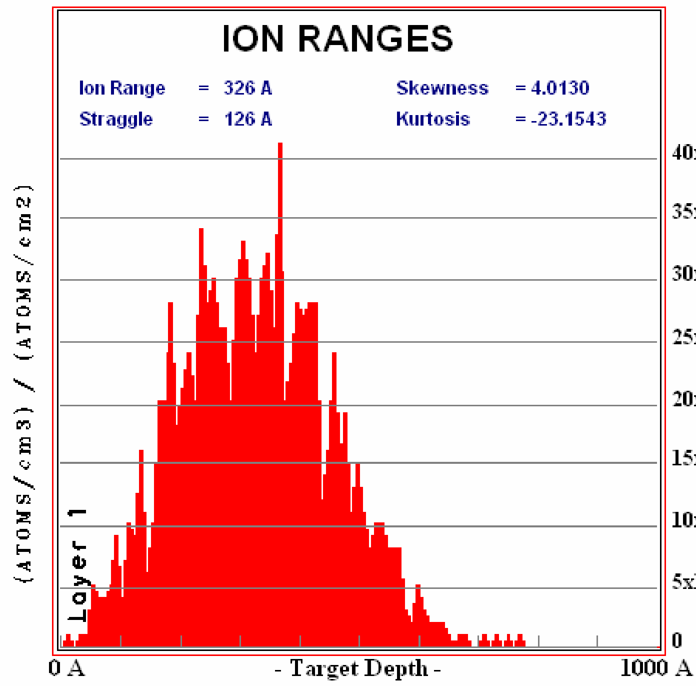

7.1 (b)

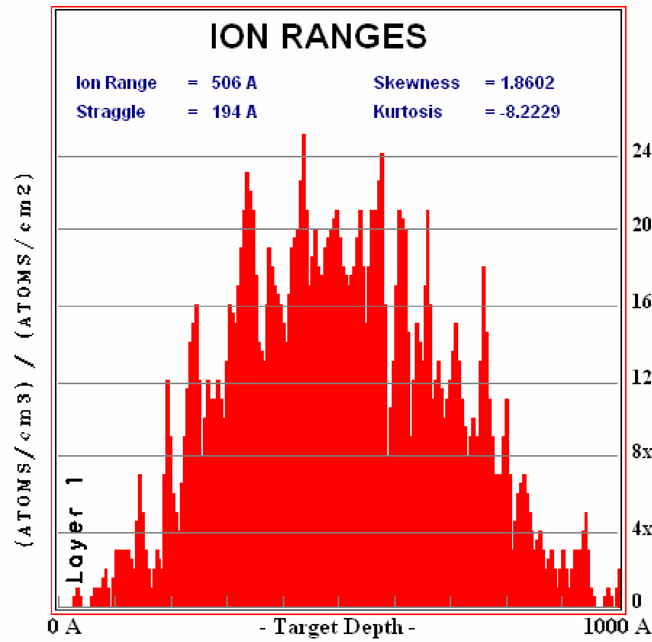

7.1 (c)

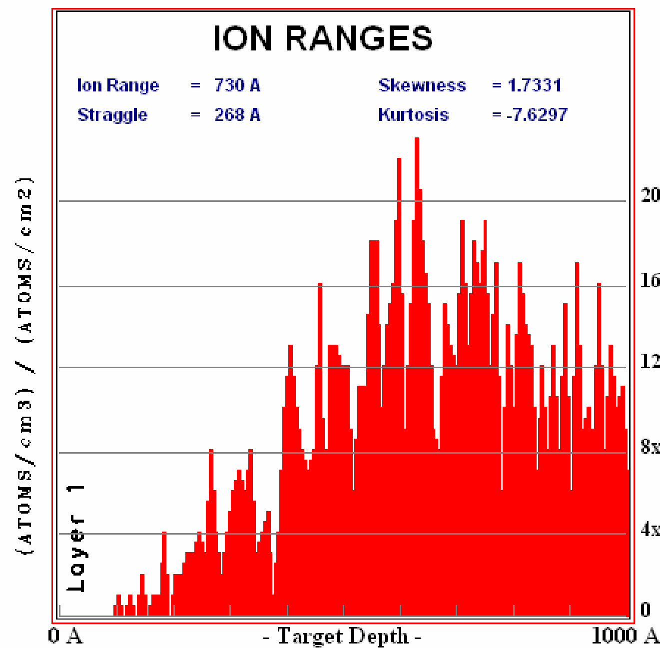

7.1 (d)

Figure 7.1. Simulation done by SRIM 2003 to calculate the In ion ranges. (a) Ion range is 20 nm when acceleration energy was 60 keV; (b) with 120 keV, it was increased to 33 nm; (c) with 200 keV, it was 51 nm; and (d) with 300 keV, ion range was 73 nm.

ions with the target lattice under different acceleration voltages of 60, 120, 200 and 300 keV, respectively. The simulations were calculated by a program called SRIM 2003 (The Stopping and Range of Ions in Matter) developed by J. F. Ziegler and J. P. Biersack. The results show that the implantation ranges of In ions were 20, 33, 51 and 73 nm, respectively. It can be seen clearly from Fig. 7.1 that elastic scattering events occurred well near the surface while acceleration energies were lower and also while the energies were larger these scattering events occurred more extensively in deeper region of the bulk ZnO. The number of collision events is indicative of the number of vacancies produced by the incident ion beam [21].

Figure 7.2 shows the experimental RBS/C spectra which illustrate the depth profile of In implanted ZnO single crystal as a function of acceleration energies. These experimental results show that the thickness of the damaged region becomes narrow as a result of increasing acceleration voltage which is completely reverse with usual trend. The damage peak height also decreases with increasing energy. However, it is difficult to draw any explanation here about these inconsistent results. Nevertheless, further RBS/C measurements with improved depth resolution may be carried out to see the actual reason.

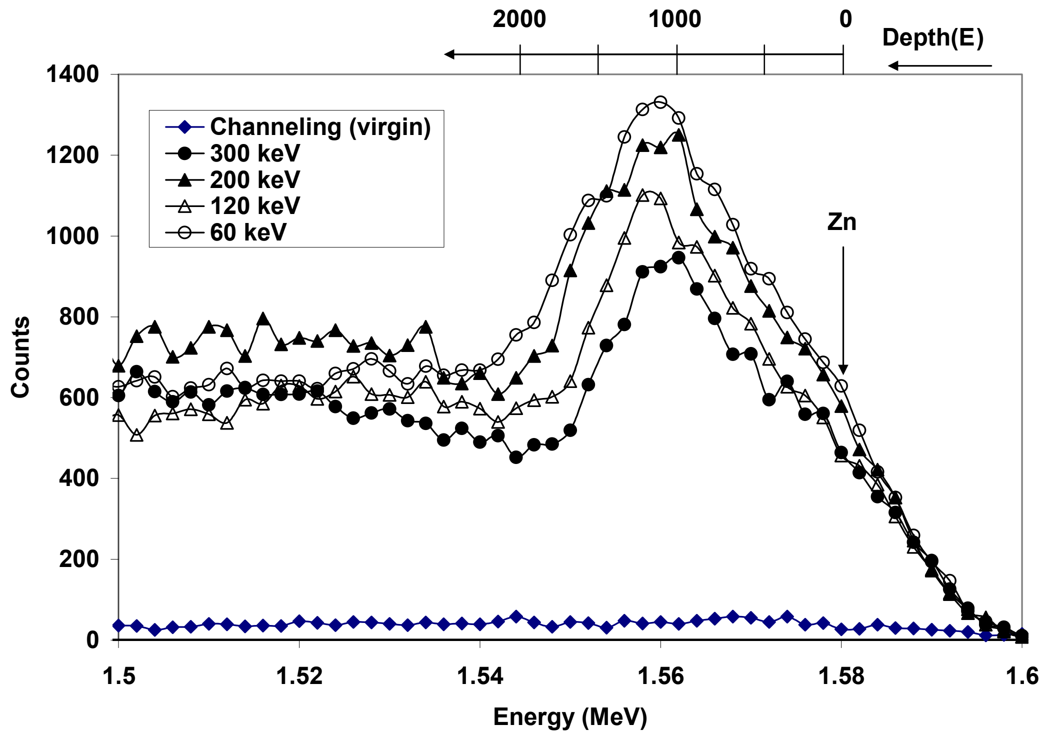

Figure 7.2 RBS/C spectra of In implanted ZnO single crystal. Implantation has been done at room temperature to a dose of 3Ч10^{14} ions/cm^{2}. Depth profile can be observed here under different acceleration voltages of 60, 120, 200 and 300 keV, respectively.

Finally, the Table 7.1 shows the results of Hall-effect measurements after In implantation into ZnO single crystal. From the following table it cab seen that the resistivity decreases with increasing annealing temperature of the implanted sample while the carrier density increases. But it shows some inconsistency about the mobility with increasing annealing temperature. These results are also not so good to predict something firmly. It may be happened due to imperfect preparation of the samples for Hall measurements. It may be

noted that the distance of the four point probe from each other should be the same, but, in this case those contacts somehow could not be done perfectly due to the smaller size of the samples. Further attempt can be made to do all those experiments carefully.

Table 7.1: Some electrical properties of In implanted single crystal ZnO

In implanted ZnO Samples	Resistivity (Ω-cm)	Carrier concentration ($/cm^3$)	Mobility ($cm^2/v\text{-}s$)
as-implanted	319.4	1.7Ч10^{14}	115
annealed (800 °C)	86.11	1.8Ч10^{15}	39.4
Annealed (1000 °C)	6.68	1.4Ч10^{16}	67.3

7.4 Conclusion

In this chapter, it is difficult to make a fruitful prediction from the above experimental results. RBS/C results reveal that the formation of surface damage layers is dependent on acceleration energy. But these results are inconsistent with the simulation one. The Hall measurements show that the carrier concentration increases and resistivity decreases as a result of increasing annealing temperatures while mobility does not show any particular trend.

7.5 References

[1] A. M. A. Rahma and T. Narusawa, J. Mater. Sci. Soc. Jpn. **45,** 6 (2008).

[2] D.C. Look, J. W. hemsky, and J. R. Sizelove, Phys. Rev. Lett. **82,** 2552 (1999).

[3] D.C. Look, J. W. hemsky, and J. R. Sizelove, Phys. Rev. Lett. **82,** 2552 (1999).

[4] K. Minegishi, Y. Koiwai, Y. Kikuchi, K. Yano, M. kasuga and A. shimizu, Jpn. J. Appl. Phys. **36,** L1453 (1997).

[5] C. Rouleau, S. Kang, D. Lowndes, unpublished.

[6] T. Yamamoto and H. Katayama-Yoshida, Jpn. J. Appl. Phys. **38,** L166 (1999).

[7] M. Joseph, H. Tabata, T. Kawai, Jpn. J. Appl. Phys. **38,** L1205 (1999).

[8] T. Aoki, Y. Hatanaka and D.C. Look, Appl. Phys. Lett. **76,** 3257 (2000).

[9] Y. R. Ryu, S. Zhu, D. C. Look, J. M. Wrobel, H. M. Jeong and H. W. White, J. Cryst. Growth. **216,** 330 (2000).

[10] T. Dietl, H. Ohno, F. Matsukura, J. Cibert and D. Ferrand, Science. **287,** 1019 (2000).

[11] K. Sato and H. Katayam-Yoshida, Jpn. J. appl. Phys. **40,** L334 (2001).

[12] K. Sato and H. Katayam-Yoshida, Jpn. J. appl. Phys. **39,** L555 (2000).

[13] K. Sato and H. Katayam-Yoshida, Physica E. **10,** 251 (2001).

[14] K. Sato and H. Katayam-Yoshida, Mater. Res. Soc. Symp. Proc. **666,** F4-6 (2001).

[15] T. Yamamoto and H. Katayama-Yoshida, Jpn. J. Appl. Phys. **38,** L166 (1999).

[16] T. Fukumura, Z. Jin, M. Kawasaki, T. Shono, T. hasegawa and S. Koshikara et. al. Appl. Phys. Lett. **78,** 958 (2001).

[17] T. wakano, N. Fujimura, Y. Morinaga N. abe A. Ashida and T. Ito, Physica E. **10,** 260 (2001).

[18] Z. Jin, K. Hasegawa, T. Fukumura, Y. Z. Yoo, T. Hasegawa and H. koinuma et. al. Physica E. **10,** 256 (2001).

[19] S. W. Jung, S. J. An, G. C. Yi, C.U. Jung, S. I. Lee and S. Cho, Appl. Phys. Lett. **80,** 4561 (2002).

[20] K. veda, H. Tabota and T. Kamai, Appl. Phys. Lett. **79,** 988 (2001).

[21] J. F. Ziegler, “SRIM Lab#2: Target Damage,” vol. 2005, pp. 6, 3/21/2005 http://www.srim.org/SRIM/Tutorials/SRIM%20 Tutorial-2%20-20Damage.pdf

CHAPTER 8

Conclusions and future directions

8.1 Conclusions

Its large band gap renders ZnO suitable for the fabrication of high-temperature, high-power devices with application, among others, in space where typical operating temperatures exceed 200 °C. Compared to other semiconductors, very little is known about defects in ZnO. This dissertation aims to investigate the damage buildup behaviour in single crystal ZnO by deposition and implantation with other elements.

In this thesis, issues relating to obtain successful fabrication of ZnO based devices have been investigated using a range of semiconductor processing and characterization techniques. Such issues include the way in which contact-induced defects affect the material, as well as implantation-induced damage in ZnO. ZnO has three key advantages. First, it is semiconductor, with a direct wide band gap of 3.37 eV and a large exciton binding energy (60 meV). It is an important functional oxide, exhibiting near-ultraviolet emission and transparent conductivity. Secondly, because of its noncentral symmetry, ZnO is piezoelectric, which is a key property in building electromechanical coupled sensors and transducers and finally, biomedical applications without coating. With these three unique characteristics, ZnO could be one of the most important nanomaterials in future research and applications.

Aside from doping and defect issues in ZnO, if devices are to be realized in this materials system, the stability and reproducibility of metal contacts must be guaranteed. However, metal contact technology in ZnO material has not been explored extensively so far. In chapter 4, a study of metallic contact to ZnO was presented as relevant to device performance. This was achieved by Ti deposition on ZnO single crystal. Mainly, it was tried to investigate the stability of Ti/ZnO interface as a function of temperature. The crystalline quality and deposition and annealing effects on the interface structure were investigated with Rutherford Backscattering Spectrometry and channeling technique using 2 MeV $^{4}He^{+}$ ion beam. After Ti deposition, the minimum yield increased from 2% to 7% for substrate ZnO which indicates that damage occurred even at room temperature by deposition due to interface reaction between Ti and ZnO. Normally it does not happen to ZnO due to deposition. The crystalline quality becomes degraded very much after annealing the sample at 300 °C as the minimum yield was found of 16%. From the RBS/C spectra for annealed sample at 400 °C, it was clear that Zn atoms had moved on the surface.

A model has been proposed as depicted in Fig. 4.8 to understand the reaction kinetics during and after deposition and atomic composition at the interface of Ti with ZnO which can be explained as follows- the oxygen atoms in ZnO substrate reacts with Ti layer to form TiO and leaves free Zn atoms behind.

Since the samples were heated in the air atmosphere, it will become stable forming TiO_2 in the interfacial region and free Zn atoms will be available onto the surface which reacts with oxygen in the air to form ZnO.

Atomic Force Microscopy was carried out to study the surface morphology, no crack was observed for as-deposited as well as annealed samples, which suggests that those Zn atoms (approximately 6.4 Ч 10^{16} atoms/cm^2) moved onto the surface due to diffusion after post-annealing of the sample at 400 $^{\circ}C$, which could lead to the degradation of the device as a result of this contact metallization.

Ion implantation is a popular and useful doping method in materials science community. Some reports already have come out suggesting that several parameters during implantation such as environment and temperature are responsible for damage buildup in the host material. Following metallic contact studies, from the above points of view, an attempt was made to investigate the influence of implantation ion current density on disorder production in ZnO which was presented in chapter 5. To do this, In^+ ions were implanted into ZnO single crystal at room temperature, under an acceleration voltage of 120 keV to a dose of 1Ч10^{15}/cm^2 with different ion current densities of 0.7 and 1.4 $\mu A.cm^{-2}$, respectively. Damage accumulation and recovery following implantation were monitored through a combination of Rutherford

backscattering spectrometry and channeling techniques. RBS/C results showed that the minimum yield, χ_{min} of the substrate ZnO single crystal increased from 2% to 22% after In^+ implantation and the formation of bulk defect was found to be dependent on implantation ion current density. Thermal treatment after ion implantation led to improve the damage recovery. Damage recovery started after annealing the sample at 600 °C and it was found that the crystallinity of ZnO appears to maximum recover following high temperature at 1000 °C, but complete recovery could not be achieved at this temperature after In^+ implantation.

RBS/C study also indicates that In atoms are located in the lattice site. In atoms started to diffuse towards the surface and segregate there during post annealing of the sample at 800 °C. After annealing at 1000 °C, there were no In atoms in the bulk single crystal ZnO but only had appeared on the surface and RBS/C results also suggested that there were no Indium desorption at this temperature.

Then the influence of ion dosage on damage formation in the bulk material and its recovery were investigated by means of RBS/C and Photoluminescence studies, respectively, that was presented in chapter 6. Three different dosages: 1Ч10^{14}, 3Ч10^{14} and 1Ч10^{15} ions.cm^{-2}, respectively, were chosen for In implantation in commercial aspects. Experimental results reveal that damage

buildup was found to be dependent on the ion dosage. The damage intensity of implanted samples gradually increased as a result of increasing ion dosage. Heat treatment after ion implantation led to improve the damage recovery as the PL intensity gradually increased with increasing temperature. After post-annealing of the implanted sample at highest temperature 1000 °C, the intensity was maximum which indicates that the damage was minimum. However, for damage recovery, the Photoluminescence study was consistent with RBS/C study. It was identified that 800 °C may be the preferred annealing temperature for ZnO, as the maximum band-edge emission occurred in the same wavelength at 375 nm for both virgin and 800 °C annealed samples.

Finally, in chapter 7, another attempt was taken to investigate the influence of accelerating energy on defects formation. For this study, In ions were implanted into (0001) zinc face ZnO at room temperature to a fluence of 3 Ч 10^{14} ions/cm^2 under different accelerating voltages of 60, 120, 200 and 300 keV, respectively. The ion beam produced depth profiles were investigated by means of Rutherford Backscattering technique in channeling mode using 2 MeV $^4He^+$ ion beam. The results reveal that the formation of surface damage layers is dependent on accelerating voltage but inconsistent with TRIM calculation. Ion ranges are 20, 32, 50 and 72 nm for 60, 120, 200 and 300 keV, respectively, calculated by SRIM 2003. On the other hand, it was observed from this RBS/C study that the thickness of damaged region becomes narrow

with increasing energy which is completely reverse with usual trend. The damage peak height also decreases as a result of increasing energy. However, we don't know the actual reason.

Then, Hall-effect measurements were carried out to investigate the electrical properties of In implanted ZnO single crystal. To do so, In ions were implanted at room temperature to a dose of 1Ч10^{15}/cm^2 with ion current density 0.7 μA/cm^2 under an acceleration voltage 120 keV. The resistivity decreased as a result of increasing temperature. On the other hand, carrier concentration increased with increasing temperature while mobility did not show any particular trend. These experimental results in chapter 7 were not so good to make a firm comment. Nevertheless, the results of this thesis may be helpful for further understanding of the necessary aspects that need to be considered when undertaking ZnO-based device fabrication.

8.2 Future directions

Whilst this thesis has addressed a number of issues in the processing and characterization of ZnO, like all investigations it has highlighted many features that are deserving of exploring. In all four major chapters, significant avenues for further study can be found and are worth exploring to gain a better understanding of the ZnO materials systems.

In chapter 4, since it was found that Ti is not suitable for metallic contact to ZnO, other experiments can be carried out to find better metallic contact to this material. In chapter 5, re-crystallization and recovery was a major issue that is worth examining in much greater detail for complete recovery. Still there is controversy to select the perfect dosage to limit the damage build-up, further study would be valuable to determine the perfect dose for ion implantation.

Given the broad field and the infancy of ZnO as a material for optoelectronics, future directions for study on this material are seemingly boundless, but will obviously be driven by demand for the successful achievement of devices. Aside from the two issues mentioned above, further study into defects in ZnO is crucial, to understand the nature of the native conductivity and why *p* type doping is difficult. A study on ion implantation as a means of achieving *p*-type ZnO would also be worth-while once the ideal conditions for minimizing degradation is identified.

8.3 Closing remarks

In closing, ZnO is a very interesting material, and is attractive for a wide range of electronic and optoelectronic devices in the blue and ultra-violet region of the spectrum. Whilst at times it presents challenges, research should enable these to be successfully overcome, enabling ZnO based devices to be realized on a commercial level. This thesis has explored a small number of issues in

ZnO by using processing and characterization techniques and has led to an increase in understanding some important features of ZnO. It is worth mentioning here that ZnO will figure strongly as a material of the future, due to its vast area of applications, and I hope the work presented in this thesis has contributed in some small way to this final goal.

List of Recent Scientific Publications and Conferences

Publications

(1) **A. M. A. Rahman** and T. Narusawa, "RBS study of Ti/ZnO interface", *Nucl. Instrum. Methods Phys. Res. B.* Vol. **266,** No. 8, 1378-1381 (2008).

(2) **Aurangzib Md. Abdur Rahman** and Tadashi Narusawa, "Effects of Ion Current Density on Defects Formation in In^+ Implanted Single Crystal ZnO", *Journal of The Materials Science Society of Japan,* Vol. 45, No. 6, 212-217 (2008).

(3) **Aurangzib Md. Abdur Rahman** and Tadashi Narusawa, "Behaviour of In^+ Implanted Single Crystal ZnO", *Journal of Applied Surface Science* (under review).

Conferences

(1) **A. M. A. Rahman** and T. Narusawa, "RBS study of Ti/ZnO interface", *18th International Conference on Ion Beam Analysis 2007,* 23-28 September, Hyderabad, India.

(2) **A. M. A. Rahman**, T. Narusawa, T. Matsuda, M. Furuta, F. Nishiyama, "RBS and channeling study of Indium implanted single crystal ZnO", *The 55th Japanese Society of Applied Physics Spring Conference 2008,* 27-30 March, Nihon University, Japan.

(3) **A. M. A. Rahman** and T. Narusawa, "Role of Ion Current Density in In^+ Implanted Single Crystal ZnO", *International Conference on Electronics, Computer and communications 2008,* 27-29 June, University of Rajshahi, Bangladesh.

(4) **A. M. A. Rahman** and T. Narusawa and T. Matsuda, "Behaviour of Indium implanted single crystal ZnO under different acceleration voltage", *The 69th Annual Meeting of Japanese Society of Applied Physics 2008,* 02-05 September, Chubu University, Japan.

(5) **A. M. A. Rahman** and T. Narusawa, "Behaviour of In^+ implanted single crystal ZnO", *The 4th Vacuum and Surface Science Conference of Asia and Australia 2008,* 28-31 October, Matsue city, Japan.

(6) **A. M. A. Rahman** and T. Narusawa and F. Nishiyama, "Depth profile of indium implanted single crystal ZnO studied by RBS/C spectrometry" *The 9th Conference on Ion Beam and Interface Analysis 2008,* 05-06 December, Kochi University of Technology, Japan.